Check for updates

Received: 30 June 2022 | Revised: 12 April 2023 | Accepted: 11 May 2023

DOI: 10.1002/hbm.26431

RESEARCH ARTICLE

WILEY

Modeling venous bias in resting state functional MRI metrics

Julia Huck[1,2] | Anna-Thekla Jäger[3,4] | Uta Schneider[3] | Sophia Grahl[3] | Audrey P. Fan[5,6] | Christine Tardif[7,8] | Arno Villringer[3,4,9,10] | Pierre-Louis Bazin[3,11] | Christopher J. Steele[3,12] | Claudine J. Gauthier[1,2,13]

[1]Department of Physics, Concordia University, Montreal, Quebec, Canada

[2]PERFORM Center, Montreal, Quebec, Canada

[3]Max Planck Institute for Human Cognitive and Brain Sciences, Leipzig, Germany

[4]Center for Stroke Research Berlin (CSB), Charité - Universitätsmedizin Berlin, Berlin, Germany

[5]Department of Biomedical Engineering, University of California, Davis, California, USA

[6]Department of Neurology, University of California, Davis, California, USA

[7]Faculty of Medicine and Health Sciences, Department of Biomedical Engineering, McGill University, Montreal, Quebec, Canada

[8]McConnell Brain Imaging Centre, Montreal Neurological Institute, Montreal, Quebec, Canada

[9]Clinic for Cognitive Neurology, University of Leipzig, Leipzig, Germany

[10]IFB Adiposity Diseases, Leipzig University Medical Centre, Leipzig, Germany

[11]Faculty of Social and Behavioural Sciences, University of Amsterdam, Amsterdam, The Netherlands

[12]Department of Psychology, Concordia University, Montreal, Quebec, Canada

[13]Montreal Heart Institute, Montreal, Quebec, Canada

Correspondence
Claudine J. Gauthier, Department of Physics, Concordia University, Montreal, QC, Canada.
Email: claudine.gauthier@concordia.ca

Funding information
Canadian Institutes of Health Research Accelerator; Canadian Natural Sciences and Engineering Research Council, Grant/Award Numbers: DGECR-2020-00146, RGPIN-2015-04665, RGPIN-2020-06812; Fonds de recherche du Québec - Nature et Technologies; Heart and Stroke Foundation of Canada, Grant/Award Number: HNC 170723; Max-Planck-Gesellschaft; Michal and Renata Hornstein Chair in Cardiovascular Imaging; National Institute of Health, Grant/Award Number: R00NS102884; Réseau en Bio-Imagerie du Quebec

Abstract

Resting-state (rs) functional magnetic resonance imaging (fMRI) is used to detect low-frequency fluctuations in the blood oxygen-level dependent (BOLD) signal across brain regions. Correlations between temporal BOLD signal fluctuations are commonly used to infer functional connectivity. However, because BOLD is based on the dilution of deoxyhemoglobin, it is sensitive to veins of all sizes, and its amplitude is biased by draining veins. These biases affect local BOLD signal location and amplitude, and may also influence BOLD-derived connectivity measures, but the magnitude of this venous bias and its relation to vein size and proximity is unknown. Here, veins were identified using high-resolution quantitative susceptibility maps and utilized in a biophysical model to investigate systematic venous biases on common local rsfMRI-derived measures. Specifically, we studied the impact of vein diameter and distance to veins on the amplitude of low-frequency fluctuations (ALFF), fractional ALFF (fALFF), Hurst exponent (HE), regional homogeneity (ReHo), and eigenvector centrality values in the grey matter. Values were higher across all distances in smaller veins, and decreased with increasing vein diameter. Additionally, rsfMRI values associated with larger veins decrease with increasing distance from the veins. ALFF and ReHo were the most biased by veins, while HE and fALFF exhibited the smallest bias.

This is an open access article under the terms of the Creative Commons Attribution-NonCommercial License, which permits use, distribution and reproduction in any medium, provided the original work is properly cited and is not used for commercial purposes.
© 2023 The Authors. *Human Brain Mapping* published by Wiley Periodicals LLC.

Across all metrics, the amplitude of the bias was limited in voxel-wise data, confirming that venous structure is not the dominant source of contrast in these rsfMRI metrics. Finally, the models presented can be used to correct this venous bias in rsfMRI metrics.

KEYWORDS
bias, rsfMRI, ultra-high field MRI, vasculature

1 | INTRODUCTION

Resting-state (rs) functional magnetic resonance imaging (fMRI) is used to measure functional connectivity and examine connectivity changes in the brain during health and disease (Lee et al., 2013). In this technique, the presence of a significant correlation between the time course of voxels in different brain regions is used to infer a functional coupling between them (Biswal et al., 1995). Functionally connected areas are characterized by high correlations between voxels in the low-frequency range (0.01–0.1 Hz) in blood oxygen-level dependent (BOLD) signal time courses. However, BOLD is a sensitive but indirect measure of neuronal activity that is predominantly based on the feed-forward blood flow response to local activity. The BOLD signal in fact reflects the dilution of deoxyhemoglobin (dHb) from veins, and animal studies have shown a moderate correlation with neuronal activity (Logothetis & Wandell, 2004; Winder et al., 2017). Because of this physiological underpinning, it is highly sensitive to local vascular properties, especially venous structure, and physiology (Tsvetanov et al., 2021). Recent research has focused on the impact of vascular physiology on the BOLD signal (Abdelkarim et al., 2019; Chen et al., 2010; Drew, 2019; Gagnon et al., 2015; Garrett et al., 2017; Gauthier et al., 2013; Kalcher et al., 2015; Liu & Li, 2016; Tsvetanov et al., 2021; Vigneau-Roy et al., 2014). For instance, Gagnon et al. used two-photon microscopy as well as an oxygen-sensitive nanoprobe to investigate the microscopic vascular behavior of the BOLD signal in rodents. They showed that venous size and orientation was an important determinant of the BOLD signal (Gagnon et al., 2015). Further, Kalcher et al. used graph clustering to identify the regions with the greatest resting state correlations with other nodes within the graph. They found that these high correlation areas overlap at more than 75% with voxels that contain large veins detected using susceptibility-weighted imaging (SWI), showing that correlations of resting state signals are biased by the presence of large veins (Kalcher et al., 2015). However, the impact of local vascular properties such as vein diameter and distance of tissue voxels to veins has not been well documented as it is typically not measured or reported. Furthermore, venous structures are highly variable across brain regions and individuals (Bernier et al., 2018a; Huck et al., 2019; Kannurpatti et al., 2010); and exhibit different anatomical and physiological coupling properties in older or diseased populations as a result of well-documented vascular changes (Dai et al., 2012; Fulop et al., 2019; Paneni et al., 2017; Plante, 2002; Sweeney et al., 2018; Xu et al., 2017).

RsfMRI can be used to compute a variety of metrics to quantify connectivity. Some of the most commonly used local rsfMRI methods include the amplitude of low-frequency fluctuations (ALFF), fractional ALFF (fALFF), regional homogeneity (ReHo), newer methods such as the Hurst exponent (HE) using Detrended Fluctuation Analysis (DFA) as well as graph-based measures such as eigenvector centrality (EC). ALFF analysis focuses on regional (voxel-wise) temporal dynamics and is predicated on the idea that higher ALFF values reflect more brain activity (Y.-F. Zang et al., 2007). fALFF is a variation of ALFF where all signals are scaled by total power across all frequencies to determine the relative contribution of different regions (J. A. Turner, 2013; Zou et al., 2008). ReHo quantifies the similarity in time course with the nearest neighbor voxels with the assumption that adjacent areas are more likely to be involved in a specific function when they exhibit similar temporal patterns (Jiao et al., 2019; Y. Zang et al., 2004). HE is used to identify the fractal properties of the BOLD signal timeseries to provide information about how self-similar the signal is across multiple time scales. Self-similarity is a relevant property of temporal signals in a wide variety of natural signals including fMRI (Hardstone et al., 2012). EC is a graph-based approach to quantify network properties of BOLD rsfMRI. EC reflects the importance of a voxel within a network, so that a voxel is attributed a large value when it shows strong correlations to other voxels that are also important and central to the network (Lohmann et al., 2010).

While the BOLD signal is sensitive to veins due to the paramagnetic effects of dHb and shows low signal in venous voxels, it cannot be used to assess venous structure because of the relatively large voxel sizes used in standard BOLD experiments (1.5–3 mm typically), since BOLD is optimized to capture temporal changes in dHb concentrations. Instead, venous structure can be imaged using higher-resolution susceptibility-based imaging techniques. These imaging techniques also rely on the paramagnetic properties of dHb to contrast veins from neighboring brain tissue. While SWI is known to have blooming effects, especially for smaller veins, the quantitative variant of this approach, called Quantitative Susceptibility Mapping (QSM), ensures an accurate estimation of vein diameters (Cetin et al., 2016; Hsieh et al., 2016; Wang & Liu, 2015). QSM has been used to identify the location and size of veins (Huck et al., 2019), and their oxygen extraction fraction (Fan et al., 2015). However, even with these techniques, modeling the brain vasculature and estimating the effects of draining veins on BOLD-derived measures is difficult due to the small size of some of the relevant veins (diameter > 10 μm–4.8 mm; Gagnon et al., 2015; Larson et al., 2020). Ultra-high field MRI allows

10970193, 0, Downloaded from https://onlinelibrary.wiley.com/doi/10.1002/hbm.26431 by MPI 374 Human Cognitive and Brain Sciences, Wiley Online Library on [23/08/2023]. See the Terms and Conditions (https://onlinelibrary.wiley.com/terms-and-conditions) on Wiley Online Library for rules of use; OA articles are governed by the applicable Creative Commons License

the acquisition of higher resolution images to better model the effects of small veins not typically visible at the resolution commonly used for BOLD fMRI.

For this study, we acquired rsfMRI BOLD and QSM images at 7 Tesla (T) in the same subjects to investigate the effects of vein distance and diameter on the different rsfMRI measures of ALFF, fALFF, ReHo, HE, and EC. Furthermore, we assessed whether these venous biases show regional heterogeneity and propose a model for correcting for these effects. The model can be applied to future research on rsfMRI connectivity to improve the physiological specificity of rsfMRI connectivity measures.

2 | METHODS

2.1 | Participants

Thirty-nine right-handed healthy participants (21 females) between the ages of 20 and 30 (24.18 ± 2.36 years) each with five scanning time points were included in this study. Participants had no history of neurological disorders and did not meet any of the regular MRI exclusion criteria. They were recruited from the database of the Max Planck Institute for Human Cognitive and Brain Sciences in Leipzig, Germany, and gave written informed consent in accordance with the Declaration of Helsinki.

2.2 | Scanning protocol

The dataset was acquired in the context of a longitudinal study, where the participants learned to perform a motor sequence. Descriptions of this data have previously been published (Huck et al., 2019; Jäger et al., 2021; Tremblay et al., 2021). Briefly, participants were trained on a motor task over a time period of 17 days. Each participant performed the task for 7 days in total, of which five daily sessions took place inside the MRI scanner (d0, d1, d2, d5, and d17). For five participants one session was omitted, and two sessions were omitted for another participant due to image artifacts. Imaging data was acquired on a 7 T MRI machine (MAGNETOM, Siemens Healthcare, Erlangen, Germany) with a 32-channel Nova head coil (NOVA Medical Inc., Wilmington MA). Four of the sequences from this study were used: a rsfMRI Echo Planar Imaging series (EPI; BOLD; Poser et al., 2010), a whole brain T1 map acquired using the MP2RAGE technique (Marques et al., 2010), a low resolution B0 field map, and a two-echo 3D Gradient Echo (GRE) FLASH (Haase et al., 1986). At the beginning of each session, auto-align was used to ensure a comparable placement of the image volume between time points. Dielectric pads were placed at the sides of the participant's head to enhance signal in the temporal lobes and the cerebellum (O'Reilly et al., 2016).

BOLD rsfMRI images from the GRE-EPI sequence were acquired for 10 min while participants were instructed to keep their eyes open and focused on a fixation cross [BOLD, voxel dimensions = $1.2 \times 1.2 \times 1.2$ mm^3, 512 whole brain volumes, Field of View (FOV) = 192×192 mm^2, slice acceleration factor: 6, 102 slices, GRAPPA factor 2, partial Fourier 6/8, Repetition Time (TR) = 1130 ms, Echo Time (TE) = 22 ms, flip angle = 40°, bandwidth = 1562 Hz/Px]. The rsfMRI data were acquired before the task was performed during each session. Uniform T1-weighted (T1w) (MP2RAGE) images were used for image registration [TR = 5000 ms, TE = 2.45 ms, voxel dimension = $0.7 \times 0.7 \times 0.7$ mm^3, matrix = $320 \times 320 \times 240$, inflow time 1 and 2 = 900 and 2750 ms, Flip angle 1 and 2 = 5° and 3°, bandwidth = 250 Hz/Px, and Time of Acquisition (TA) = 10:57 min]. The FLASH images used to generate QSM images were stored uncombined for each coil channel. Because there is a phase offset between the channels, the phase offset for each channel was calculated using low-resolution field maps. The phase offset maps were then registered and subtracted from the high-resolution FLASH images. Here, low-resolution field maps [TR = 18 ms, TE = 4.08 and 9.18 ms, matrix = $128 \times 128 \times 80$, flip angle = 10°, voxel dimension = $2 \times 2 \times 2$ mm^3, bandwidth = 300 Hz/Px, and TA = 3:24 min] were used to estimate the phase offset between the channels (Deistung et al., 2013; Hammond et al., 2008). The first echo of the multi-echo 3D FLASH images [TR = 29 ms, TE1 and TE2 = 8.16 and 18.35 ms, voxel dimensions = $0.6 \times 0.6 \times 0.6$ mm^3, matrix = $260 \times 320 \times 256$, GRAPPA acceleration = 3, bandwidth = 250 Hz/Px, and TA = 14:22 min] was flow compensated along all three axes and used for the QSM reconstruction.

2.3 | Image processing: rsfMRI preprocessing and feature extraction

A preprocessing pipeline, which was optimized for 7 T data, was used on the rsfMRI data (Huntenburg et al., 2018). Preprocessing consisted of removing the first five TRs to allow for signal stabilization, motion correction with Nipy's (Millman & Brett, 2007) SpaceTimeRealign (Roche, 2011) function implemented in Nipype (Gorgolewski et al., 2011), fieldmap unwarping with FSL FUGUE (Jenkinson et al., 2002), nuisance regression including image intensity and motion outliers with Nipype's ArtefactDetect, as well as white matter and cerebrospinal fluid signal regression using the CompCor algorithm (Behzadi et al., 2007) implemented in Nilearn's high_variance_confounds (Abraham et al., 2014), bandpass filtering (0.01–0.1 Hz), spatial smoothing with a 2.4 mm sigma Gaussian kernel and registration to 1.2 mm isotropic MNI space (details of the registration are in Section 2.5).

The local feature maps [ALFF, fALFF, Kendall's Coefficient Concordance (KCC) ReHo and Coherence (Cohe)-ReHo] were created with the REST toolbox (Biswal et al., 1995; Song et al., 2011) implemented in MATLAB. The bandpass filter was set to 0.01–0.1 Hz with a TR of 1.13 s for all four metrics. For the ReHo maps a cluster size of 27 voxels was used.

DFA was used to quantify the temporal self-similarity of the time series data, which was reported as the HE (Hurst, 1951). DFA computes the least squares fit of the log–log relationship between the number of time series samples in a given window (n) and the mean

10970193, 0, Downloaded from https://onlinelibrary.wiley.com/doi/10.1002/hbm.26431 by MPI 374 Human Cognitive and Brain Sciences, Wiley Online Library on [23/08/2023]. See the Terms and Conditions (https://onlinelibrary.wiley.com/terms-and-conditions) on Wiley Online Library for rules of use; OA articles are governed by the applicable Creative Commons License

standard deviation of linearly detrended windows of data of size n [Peng et al., 1994; for a comprehensive overview, see Hardstone et al. (2012)]. The standard deviation was computed for a range of window sizes n, and the slope of the least squares fit line between the log(n) and log (standard deviation) measures were calculated as the HE. For fitting, we used 15 log-spaced windows ranging from 10 to 55 samples per window.

The EC maps were generated with the fastECM algorithm (Wink et al., 2012) in MATLAB (2017b).

2.4 | Vessel segmentation

The phase images from each channel were recombined offline using the phase estimates from the low-resolution field maps to ensure a high phase image quality for QSM reconstruction. QSM images were reconstructed using the Total Generalized Variation (TGV) technique (Langkammer et al., 2015). A brain mask based on magnitude images was used for QSM reconstruction. A multiscale recursive ridge vessel filter was used to extract bright tubular structures from the QSM (Bazin et al., 2016; Huck et al., 2019). The filter extracts vessels by using a ridge filter recursively to extract 2D and 1D ridges, where 1D ridges are considered as vessels. In the first step, the vessel filter searches for the minimum difference between a plane at position x perpendicular to the direction d and the planes at $x - d$ and $x + d$ in the same direction to find the minimum contrast between the plane and its neighboring planes. The step is repeated for all 13 discrete directions. The plane with the highest contrast is chosen. This approach is repeated in the second step, where the search planes are replaced by lines. Ridge filtering is performed over multiple scales defined by Gaussian smoothing (in this work, from 1 to 4 mm FWHM), and the maximum response is kept. The filter response is converted into probability scores while considering outliers and null distributions, and voxel-wise probabilities are propagated along the ridge direction with a diffusion process. Since the basal ganglia system has a high iron content and is likely to be detected by the vessel filter as veins, the ATAG atlas (Keuken et al., 2014) was used as an exclusion prior during the vessel segmentation. Segmented vessels with a final probability above 0.5 are kept, and vessel diameter is estimated by modeling the vessel locally as a tubular structure and optimizing over centerline location and diameter to match local intensity differences in and around the detected vessel (Woerz & Rohr, 2004). Finally, the tubular model was used to derive partial volume (PV) maps indicating the estimated volume of vasculature in each voxel.

Veins with a calculated diameter smaller than 0.3 mm were excluded, since smaller vessels cannot reliably be quantified using this technique. Some surface larger veins like the sagittal and transverse sinuses were partly cropped out by the brain mask used for QSM reconstruction, therefore diameter estimations in these veins could be underestimated. However, other larger veins such as the straight sinus can be fully segmented. To understand how rsfMRI metrics are influenced by vein size and distance to veins, distance and propagated diameter maps were generated. Distance maps, indicating the distance to the nearest vein, were calculated from PV images, and the diameter of each vein was propagated to neighboring regions (up to 10 mm) until it encountered the propagated diameter of another vein (Figure 1). This process therefore ascribes a diameter and a distance to all voxels within the brain, so that the distance and diameter of the closest vein is known for every voxel in the rsfMRI metric map. Vessel filtering, distance maps, and diameter propagation were all performed in Nighres (Huntenburg et al., 2018). The propagated diameter maps and distance maps were masked to the grey matter (GM) after their registration into MNI152 space.

2.5 | Registration

To bring the rsfMRI-derived measures and the segmented veins from their native space to a common space, registrations were performed using the Advanced Normalization Tools (ANTs) software (Avants et al., 2009). Registration was divided into three steps: (1) T1w native space to MNI; (2) QSM native space to T1w native space; (3) rsfMRI native space to T1w native space. Deformation fields from Steps 1 and 2 were concatenated to bring the distance maps and propagated diameter maps from native QSM space to MNI152 space. The deformation fields from Steps 1 and 3 were concatenated to bring the rsfMRI metrics to MNI152 space.

1. A two-level nonlinear registration was used to bring the T1w images from native space to a group template (https://github.com/CoBrALab/twolevel_ants_dbm; Manera et al., 2019). During the first level, the five scans of each participant were nonlinearly registered across days into an average individual subject space. In the second level, the data were registered from the individual subject spaces across participants into a study-specific group space. The resulting group space template was then nonlinearly registered to a 1.2-mm isotropic down-sampled version of the MNI152 template (version: ICBM2019b).
2. For the registration of the distance and diameter maps, the GRE magnitude images were registered linearly to the T1w images for each day of each participant.
3. The registration of the rsfMRI images to T1w space required an initial linear registration to coarsely align the rsfMRI images to the masked MP2RAGE UNI images, followed by a nonlinear registration.

The deformation fields from the GRE magnitude and rsfMRI images were concatenated with the deformation fields from the T1w to MNI space registration (GRE magnitude/rsfMRI → T1w → subject space → group space → MNI space). During the registration, warping finer structures such as vessels can lead to incorrect values. To avoid this, the concatenated deformations from GRE magnitude/rsfMRI to MNI were applied to the propagated diameter and distance maps and rsfMRI metric maps to bring all images into the same final space. Intra-subject variability of the propagated diameter maps and distance maps were generated by calculating the mean of the standard deviations across days, and inter-subject variability maps were calculated

10970193, 0, Downloaded from https://onlinelibrary.wiley.com/doi/10.1002/hbm.26431 by MPI 374 Human Cognitive and Brain Sciences, Wiley Online Library on [23/08/2023]. See the Terms and Conditions (https://onlinelibrary.wiley.com/terms-and-conditions) on Wiley Online Library for rules of use; OA articles are governed by the applicable Creative Commons License

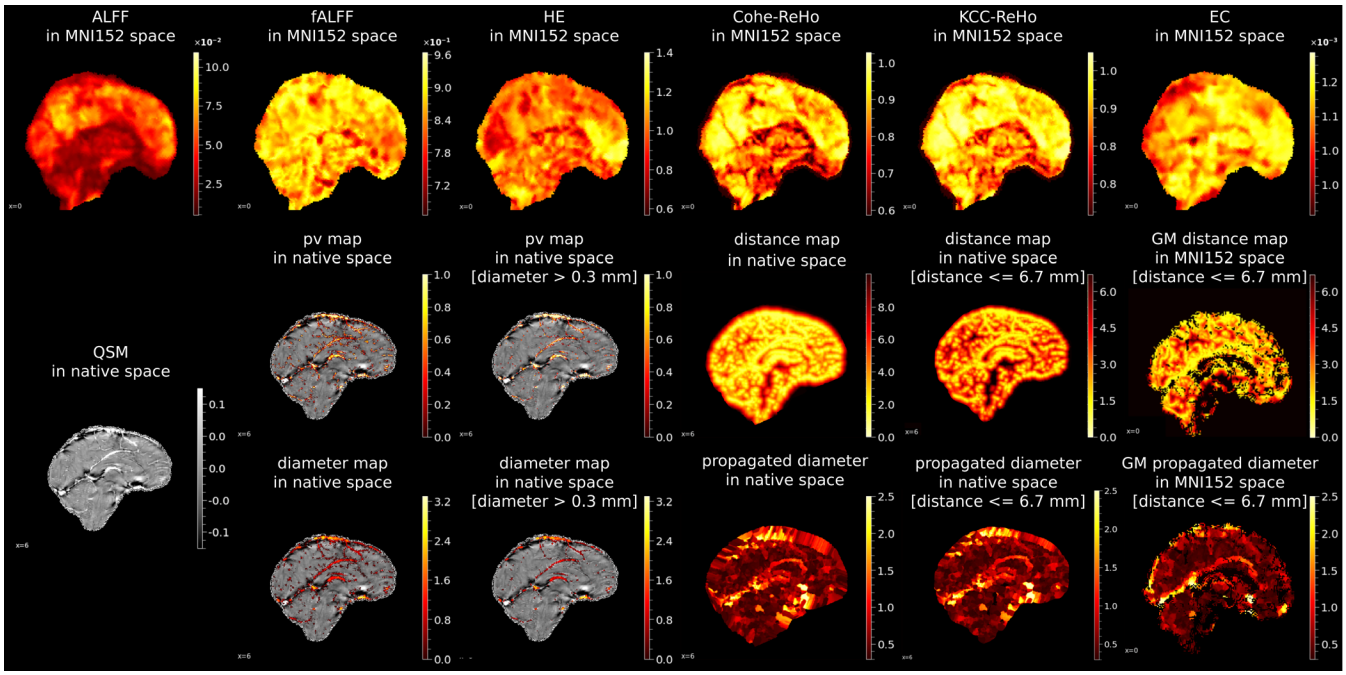

FIGURE 1 Overview of the rsfMRI metrics in MNI152 space and the processing pipeline of the QSM images. The distance maps and the propagated diameter maps were generated in native space from the veins extracted from the QSM images. The images were then registered to MNI152 space. The top row depicts the rsfMRI metrics in MNI152 space: sagittal view of the amplitude of low-frequency fluctuations (ALFF), fractional ALFF (fALFF), Hurst Exponent (HE), Coherence [Coherence (Cohe)-Regional Homogeneity (ReHo)], Kendall's Coefficient Concordance (KCC)-ReHo and Eigenvector Centrality (EC) values for one participant. *Bottom rows*: Quantitative Susceptibility Mapping (QSM) image of the same participant in native space with the resultant partial volume (PV; second row) and diameter map (third row) from the vessel segmentation filer (threshold = 0.5; native space). PV and diameter maps excluded all veins <0.3 mm. Distance map and propagated diameter map were calculated from the PV and diameter maps in native space, respectively. Tissue voxels with a distance >6.7 mm were excluded in both images. Maps were registered to MNI152 space and restricted to the GM (last column in the second and third row).

by taking the standard deviation of the mean values across days (Figure 2).

2.6 | Analyses

The analysis of the relationship between veins and rsfMRI signals was restricted to voxels with nonzero rsfMRI feature values. To predict the influence of vein diameter and vein distance, models were generated from binned data, where the rsfMRI values of the different metrics were averaged first across days and then across participants. To avoid a sparse amount of data in some bins at the extremes, the bin edges were set to 5%–95% of the propagated diameter and distance maps (resulting in 0–6.7 mm distance and 0.3–2.5 mm diameters; See Figure S2 for a visualization of density for all bins). Diameters smaller than 0.3 mm were excluded, and diameters larger than 2.5 mm were included in the last bin. The data were divided into 10 diameter bins [0.3–2.5+ mm; 0.22 mm steps] and 10 distance bins (0–6.7 mm; 0.67 mm steps). For each of these bins, the rsfMRI features were averaged first across days and then across participants (Figure 3a). The analysis was done within the whole GM voxels (whole brain), as well as for each of the seven networks of the Yeo functional connectivity parcellations (Yeo et al., 2011; Supporting Information) including the visual, somatomotor, dorsal attention, ventral attention, limbic, frontoparietal, and default mode networks. To predict the rsfMRI features using the vein diameter and distance to veins, the 100 binned values (10 diameter × 10 distance bins) were used to generate a model for diameters (x_1) and distances (x_2) separately ($\alpha x_1 + c$; and $\alpha x_2 + c$), a linear ($\alpha x_1 + \beta x_2 + c$) and higher order polynomial model (up to the fourth order; Figure 3b):

$$\text{Second order}: c + \alpha x_1 + \beta x_2 + \gamma x_1^2 + \delta x_1 x_2 + \epsilon x_2^2,$$

$$\text{Fourth order}: \zeta x_1^3 + \eta x_1^2 x_x + \theta x_1 x_2^2 + \iota x_2^3 + \kappa x_1^4 + \lambda x_1^3 x_2 + \mu x_1^2 x_2^2 + \nu x_1 x_2^3 + \xi x_2^4,$$

where α, β, γ, δ, ϵ, ζ, η, θ, ι, κ, λ, μ, ν, and ξ represent the coefficients and c the intercept of the model for the GM (Table 1). To evaluate the best fitting model, a likelihood ratio test (LRT) using the ANOVA function in R and Bayesian Information Criterion (BIC) was performed (RStudio version 1.3.1073) (Table S1 and Table 2). The model that had the last largest improvement in BIC in the polynomial models (smaller BIC values compared to the lower order model; Table 2 and Figure S3) with additionally a significantly better fit when compared to immediately lower and higher complexity models (ANOVA) was chosen. After a model evaluation, the best fitting was then applied voxel-wise to each individual participant for all 5 days in each rsfMRI metric (Figure 3c). The voxel-wise difference between the original and the predicted values was calculated to yield the residuals. Since the residuals were smaller than the measured rsfMRI values, the mean

10970193, 0, Downloaded from https://onlinelibrary.wiley.com/doi/10.1002/hbm.26431 by MPI 374 Human Cognitive and Brain Sciences, Wiley Online Library on [23/08/2023]. See the Terms and Conditions (https://onlinelibrary.wiley.com/terms-and-conditions) on Wiley Online Library for rules of use; OA articles are governed by the applicable Creative Commons License

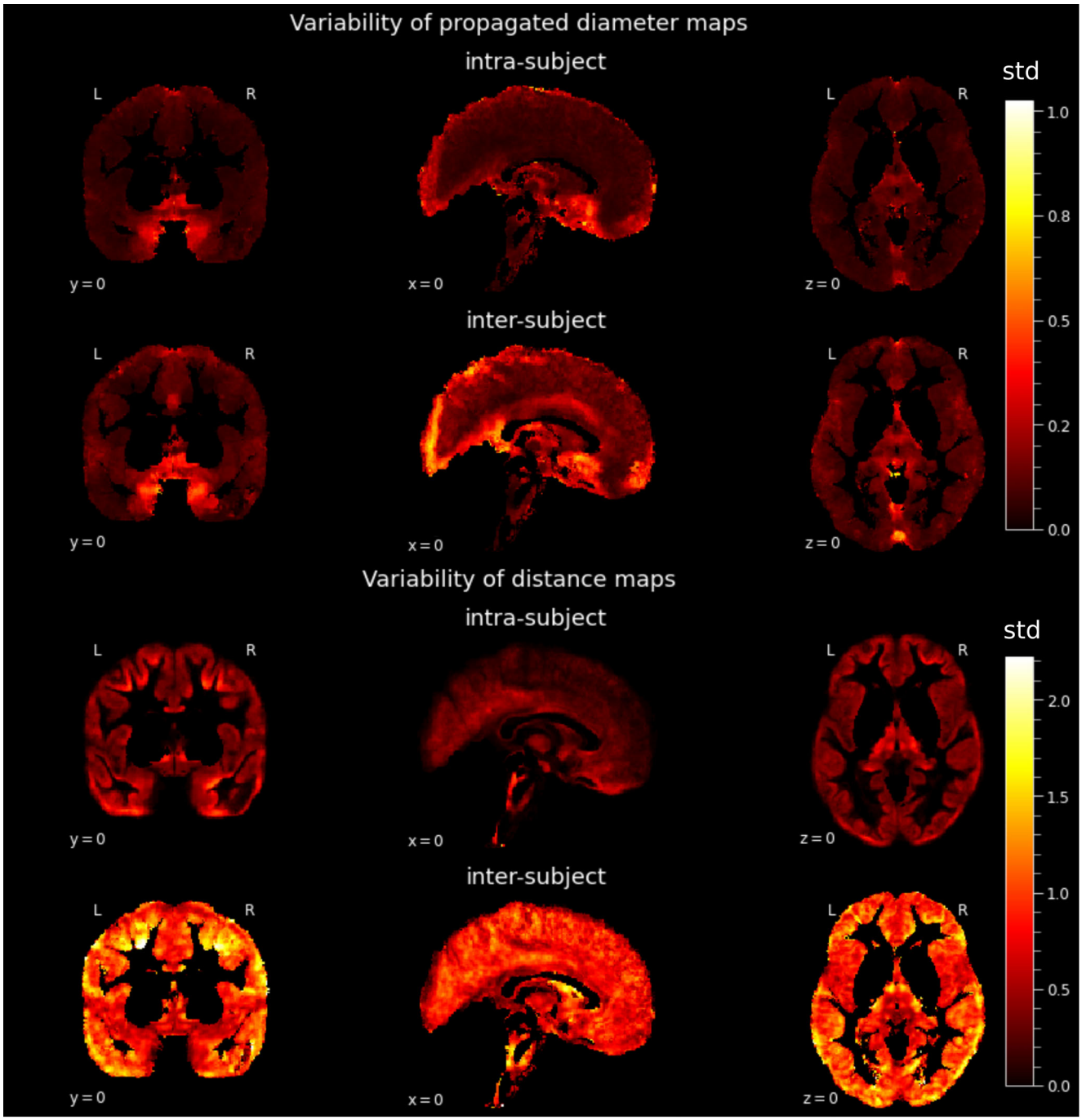

FIGURE 2 Reliability measure of propagated diameter (top) and distance maps (bottom) for participants across days (intra-subject variability) and across participants (inter-subject variability).

value of the rsfMRI GM was added as baseline to the residuals to bring the residuals to a comparable magnitude as the rsfMRI values for ease of visualization. The predicted and residual voxel-wise values were binned and averaged across days and participants and displayed as heat maps (Figures 3d and 5). Further, the voxel-wise maps of the rsfMRI metrics, the predicted values, and residuals were averaged across days and participants (without binning) and depicted as brain surface plots (Figures 3e and 8) using Nilearn 0.7.1 in python 3.8.5. A voxel-wise percentage change between the residuals and the measured data was calculated to better quantify the bias caused by the presence of veins. The R^2 values were calculated using the coefficient of determination r2_score function from sklearn in python.

3 | RESULTS

3.1 | Venous properties

A voxel-wise average of the propagated diameter maps and distance maps across participants is shown in Figure 4. The averaged

10970193, 0, Downloaded from https://onlinelibrary.wiley.com/doi/10.1002/hbm.26431 by MPI 374 Human Cognitive and Brain Sciences, Wiley Online Library on [23/08/2023]. See the Terms and Conditions (https://onlinelibrary.wiley.com/terms-and-conditions) on Wiley Online Library for rules of use; OA articles are governed by the applicable Creative Commons License

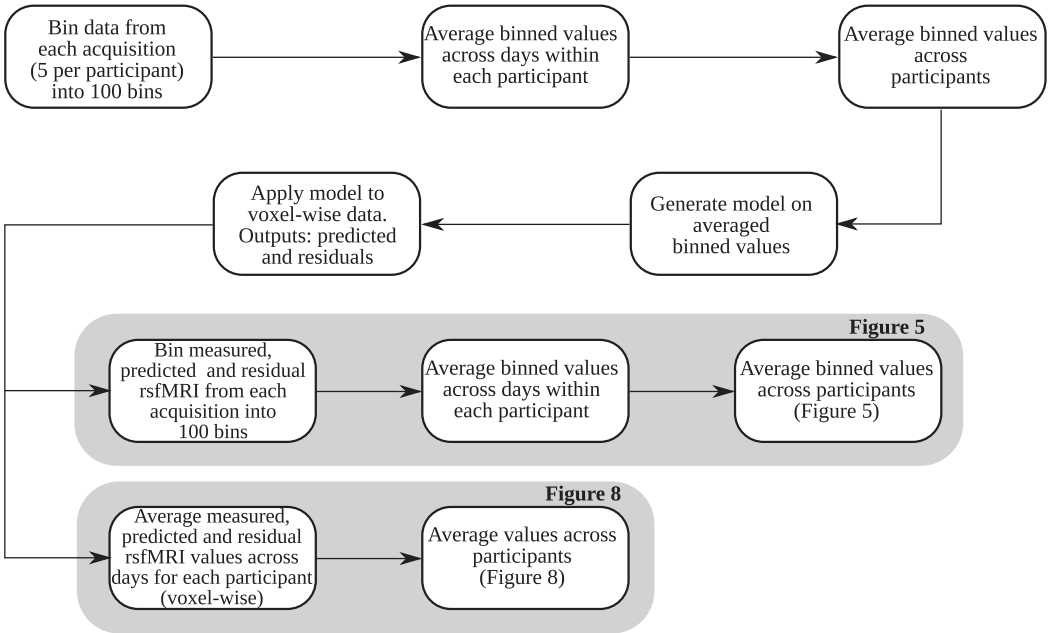

FIGURE 3 Schematic overview of the analysis pipeline. In the first step, the rsfMRI values from all acquisitions (5 per participant) were divided into 100 bins. Binned values were then averaged across days and then participants (first row). The pooled binned data were used to generate a model of the relationship between vein size and distance with each rsfMRI metric. This model was applied voxel-wise to each day of each participant (second row). The resulting predicted and residual values were divided into the same 100 bins as the original rsfMRI values, averaged across days, and participants are plotted in Figure 5 (third row). In addition, after the model was applied voxel-wise to the data, the predicted and residual values were averaged voxel-wise across days and then participants and are depicted in Figure 8 (fourth row) to show spatial patterns.

TABLE 1 Coefficients of the fourth-order polynomial model for ALFF, fALFF, HE, Cohe-ReHo, and KCC-ReHo, and EC (A + B).

(A) Second-order polynomial

	R^2	c	α	β	γ	δ	ϵ
ALFF	0.994	3.08×10^{-2}	1.63×10^{-4}	6.54×10^{-2}	-4.65×10^{-4}	4.62×10^{-3}	-1.13×10^{-1}
fALFF	0.993	8.79×10^{-1}	-6.37×10^{-4}	4.14×10^{-2}	-1.41×10^{-4}	6.67×10^{-3}	-8.21×10^{-2}
HE	0.986	9.70×10^{-1}	4.81×10^{-3}	1.70×10^{-1}	-3.33×10^{-3}	3.83×10^{-3}	-2.84×10^{-1}
Cohe-ReHo	0.991	7.70×10^{-1}	-1.83×10^{-2}	4.84×10^{-1}	-4.01×10^{-3}	8.47×10^{-2}	-9.45×10^{-1}
KCC-ReHo	0.989	8.42×10^{-1}	-1.70×10^{-2}	4.14×10^{-1}	-5.19×10^{-3}	8.27×10^{-2}	-8.34×10^{-1}
EC	0.987	1.08×10^{-3}	-4.15×10^{-6}	1.42×10^{-4}	8.32×10^{-8}	1.10×10^{-5}	-2.12×10^{-4}

(B) Fourth-order polynomial

	ζ	η	θ	ι	κ	λ	μ	ν	ξ
ALFF	9.84×10^{-5}	-1.37×10^{-3}	-2.23×10^{-4}	6.18×10^{-2}	-5.99×10^{-6}	6.84×10^{-5}	2.89×10^{-4}	-5.07×10^{-4}	1.10×10^{-2}
fALFF	3.95×10^{-5}	-1.35×10^{-3}	-3.15×10^{-3}	4.77×10^{-2}	2.20×10^{-7}	5.99×10^{-5}	2.90×10^{-4}	3.81×10^{-4}	-8.91×10^{-3}
HE	5.67×10^{-4}	-8.41×10^{-4}	-1.39×10^{-4}	1.50×10^{-1}	-3.10×10^{-5}	-1.94×10^{-6}	3.64×10^{-4}	-7.08×10^{-4}	-2.57×10^{-2}
Cohe-ReHo	2.51×10^{-3}	-2.29×10^{-2}	4.61×10^{-3}	5.12×10^{-1}	-2.32×10^{-4}	7.82×10^{-4}	5.25×10^{-3}	-1.10×10^{-2}	-8.57×10^{-2}
KCC-ReHo	3.12×10^{-3}	-2.35×10^{-2}	1.16×10^{-2}	4.42×10^{-1}	-2.97×10^{-4}	7.55×10^{-4}	5.57×10^{-3}	-1.34×10^{-2}	-7.04×10^{-2}
EC	1.35×10^{-7}	-2.70×10^{-6}	-2.90×10^{-6}	1.16×10^{-4}	-5.33×10^{-9}	-1.16×10^{-8}	1.02×10^{-6}	-5.97×10^{-7}	-2.14×10^{-5}

propagated diameter maps show that most voxels are located in the vicinity of smaller veins (diameter < 0.48 mm). The mean and standard deviation of segmented vein diameters for all participants and days is 1.05 ± 0.61 mm. Veins of larger diameters are observed mostly in areas where the straight, sagittal, and transverse sinuses are located. Furthermore, sulcal voxels were found to be typically located closer to

10970193, 0, Downloaded from https://onlinelibrary.wiley.com/doi/10.1002/hbm.26431 by MPI 374 Human Cognitive and Brain Sciences, Wiley Online Library on [23/08/2023]. See the Terms and Conditions (https://onlinelibrary.wiley.com/terms-and-conditions) on Wiley Online Library for rules of use; OA articles are governed by the applicable Creative Commons License

TABLE 2 BIC values of each model; values in bold denote the BIC value with the largest changes compared to the direct lower model.

	Diameter	Distance	Linear	Second order	Third order	Fourth order	Fifth order	Sixth order	Seventh order	Eighth order
ALFF	−876.03	−752.18	−919.71	−978.16	−1007.35	**−1187.26**	−1199.76	−1233.33	−1226.80	−1223.51
fALFF	−877.49	−715.00	−918.64	−999.42	−1026.39	**−1134.91**	−1126.55	−1116.38	−1087.87	−1061.12
HE	−695.96	−526.27	−731.37	−770.10	−813.51	**−885.37**	−893.20	−914.55	−916.68	−911.64
Cohe-ReHo	−400.76	−321.70	−397.58	−513.28	−548.60	**−732.66**	−738.94	−777.60	−782.84	−778.39
KCC-ReHo	−386.51	−337.72	−382.55	−516.04	−553.44	**−726.48**	−740.87	−789.34	−799.03	−797.72
EC	−2092.09	−2072.86	−2212.49	−2244.40	−2241.44	**−2404.32**	−2400.38	−2419.49	−2423.00	−2414.45

Note: BIC values of each model; values in bold denote the BIC value with the largest changes compared to the direct lower model (see Fig. S3 in the supplementary material as visualization of the BIC values).

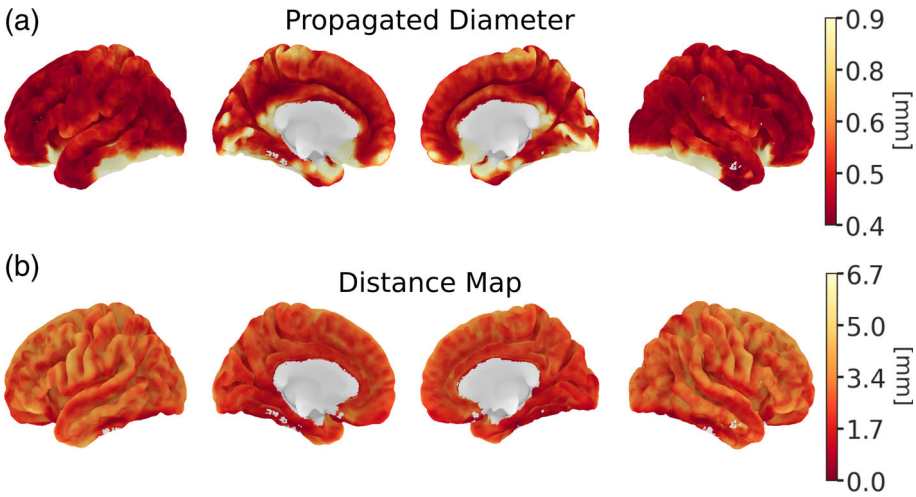

FIGURE 4 Propagated diameter maps and distance maps were averaged voxel-wise across days and then across participants. The average data is depicted as brain surface plots. Panel (a) shows that the distribution is fairly uniform over the brain, with most regions being close to veins of smaller diameters (darker red). Panel (b) shows a pattern whereby regions along the midline are closer to veins (darker red), while there appears to be more spatial variability in distance on the external cortical surface with veins further away from veins, especially along gyri (light yellow).

veins, while gyral voxels were located further from veins in the distance map.

3.2 | Venous bias model

The relationship between binned values for all metrics and vein diameter and distance is depicted in Figure 5. These binned values were used to generate a linear model and a higher-order polynomial model (coefficients Table 1) within the GM. A model comparison with LRT (ANOVA function in R) and BIC (Tables S1 and 2) showed that for all models the fourth-order polynomial model provided the best improvement in BIC with a significantly better fit compared to the third-order polynomial model ($p < .001$). While the BIC values continue to decrease after the fourth polynomial model, the decrease was small, and values seemed to reach a plateau. To avoid overfitting, the fourth-order polynomial model was chosen for all metrics. The outputs of the models are shown in Figure 5, with plots showing the binned measured rsfMRI metric values (left column), the binned predicted values (middle column), and the binned residuals across the entire GM (right column). Similar plots for the seven rsfMRI networks of the binned rsfMRI metric values are depicted in Figure S1.

The measured and predicted values for ALFF, fALFF, HE, and EC showed a similar gradient-like pattern with two main distinct features. Values were higher across all distances in small compared to large veins, and decreased with increasing vein diameter. Additionally, rsfMRI values associated with larger diameter veins decrease with increasing distance from the veins.

Both ReHo metrics, KCC, and Cohe, show low values close to veins (for diameters 1.14–2.06 mm) in addition to low values in voxels further away from big veins. The R^2 values in Table 1 measure the fit of the model on the binned data, without considering the variability of the true rsfMRI values. In all cases, the model shows a good fit to the average binned data (R^2 values in Table 1).

Residuals show a relative uniform pattern and higher overall rsfMRI values due to the addition of the GM mean as baseline.

3.3 | Voxel-wise venous bias

To examine how predictive the model is locally, 2D histograms of the predicted versus measured voxel-wise values were generated and are shown in Figure 6. The range of predicted values was found to be smaller than the range of values for all metrics. In the 2D histograms comparing predicted and actual values, the highest densities between rsfMRI and predicted values have a flat profile for ALFF and fALFF, while HE, and EC show a higher density cluster in the middle and KCC-ReHo and Cohe-ReHo at higher values. The model was found to

10970193, 0, Downloaded from https://onlinelibrary.wiley.com/doi/10.1002/hbm.26431 by MPI 374 Human Cognitive and Brain Sciences, Wiley Online Library on [23/08/2023]. See the Terms and Conditions (https://onlinelibrary.wiley.com/terms-and-conditions) on Wiley Online Library for rules of use; OA articles are governed by the applicable Creative Commons License

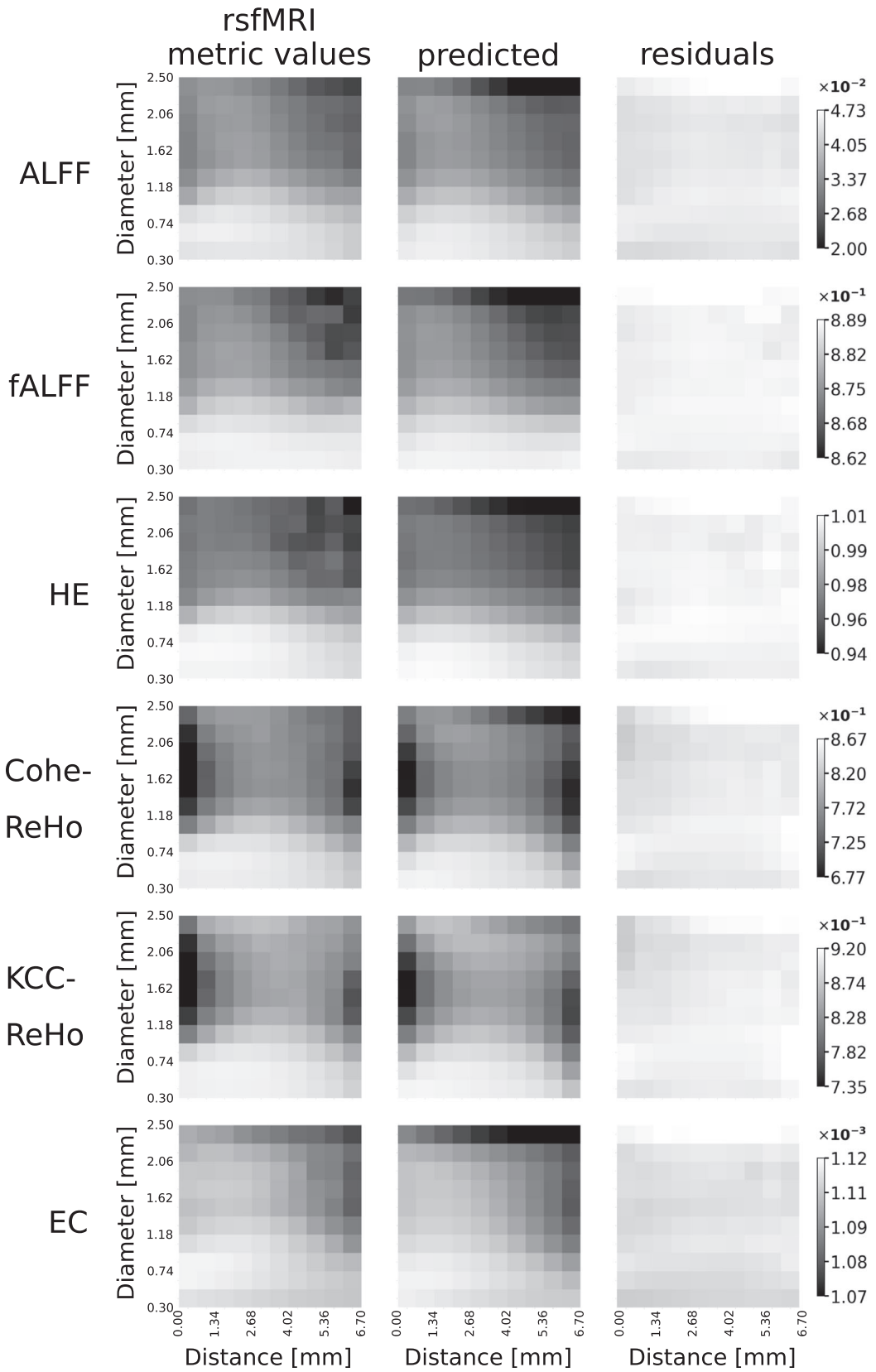

FIGURE 5 rsfMRI data for ALFF, fALFF, HE, KCC-ReHo, Cohe-ReHo, and EC averaged according to the diameter and distance to the closest vein. Values are binned (100 bins) for 10 distances (0–6.7 mm) and 10 diameter ranges (0.3–2.5+ mm). The binned measured rsfMRI values were used for each metric to generate a model. The model was applied voxel-wise and the resulting predicted and residual values were binned and averaged (depicted in the second and third column for each metric). Mean GM value was added back to the residuals for visualization only, to bring all quantities on the same scale.

10970193, 0, Downloaded from https://onlinelibrary.wiley.com/doi/10.1002/hbm.26431 by MPI 374 Human Cognitive and Brain Sciences, Wiley Online Library on [23/08/2023]. See the Terms and Conditions (https://onlinelibrary.wiley.com/terms-and-conditions) on Wiley Online Library for rules of use; OA articles are governed by the applicable Creative Commons License

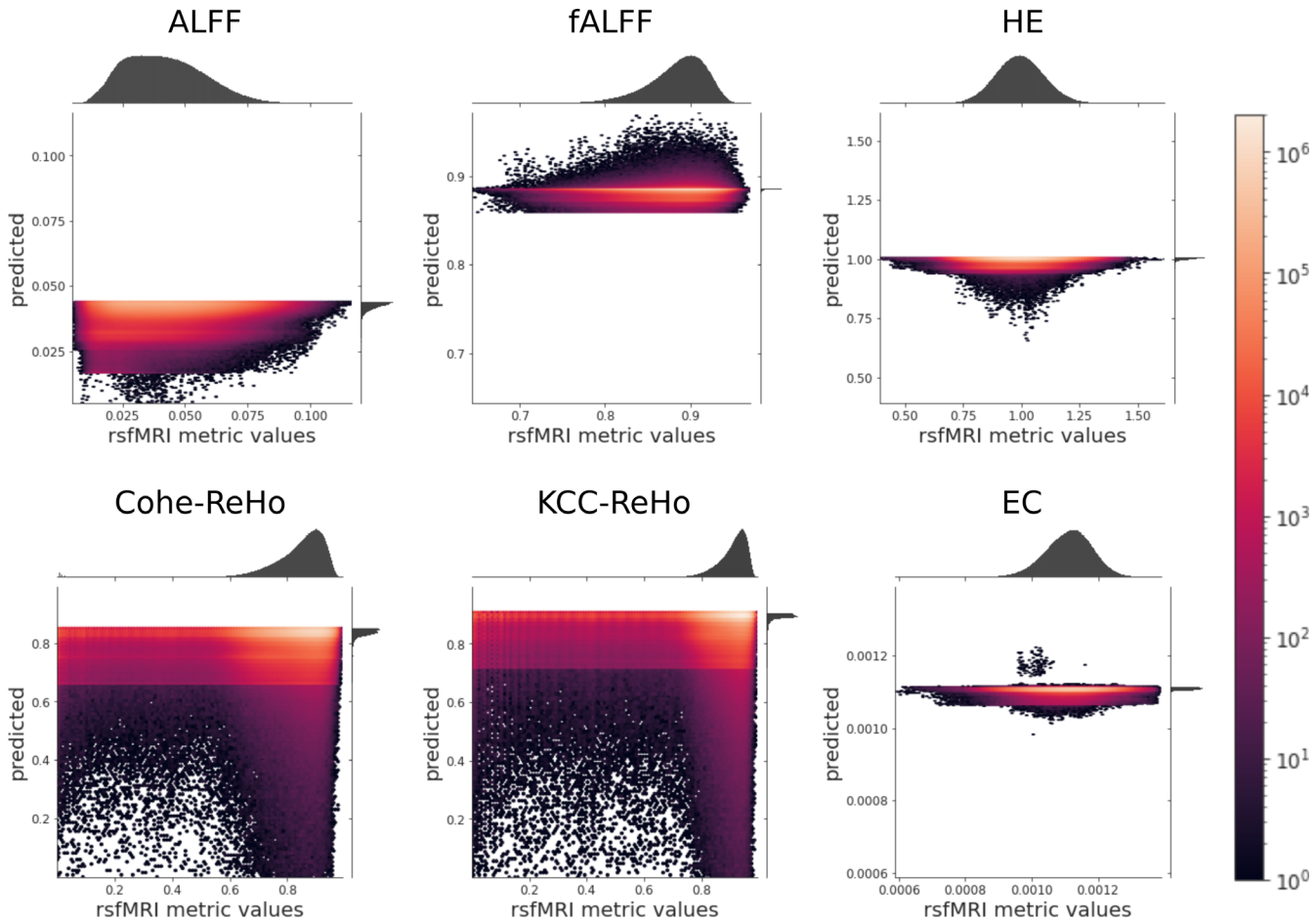

FIGURE 6 2D histograms of the measured and predicted values. The figure shows the distribution of the values of the measured rsfMRI values compared to the predicted values of the model. The 1D histogram of measured and predicted values is shown on the top and right sides of each graph, respectively. The graphs show a narrower distribution for predicted values as compared to measured values, showing that venous structure explains only part of rsfMRI metrics.

predict predominantly lower values for ALFF, but higher values for fALFF, KCC-ReHo, and Cohe-ReHo. HE and EC predictions show a more normal distribution close to the mean of their data range.

The R^2 values for the correlation between measured and predicted rsfMRI metric values calculated individually for each participant and day ranged between 4.89×10^{-9} and 0.12 and are represented in Figure 7. Overall, the vascular model does not predict a large portion of the actual rsfMRI metrics values at the individual voxel-wise level, indicating that the corresponding bias is systematic, but limited.

3.3.1 | Spatial pattern of venous bias

Voxel-wise averages across days and participants for (1) rsfMRI metrics values, (2) predicted values from the group-based GM model, (3) residuals, and (4) a percentage difference between the rsfMRI values and the residuals are mapped on the surface in Figure 8. Residuals describe the rsfMRI metric values without the venous component calculated by the model. Overall, the voxel-wise predicted values did not show any common specific spatial pattern across metrics, showing a relatively spatially uniform relationship between vein diameter and rsfMRI metrics, and the residuals showed similar spatial patterns to the original rsfMRI metric values.

The percentage change quantifies the relative amount of signal veins that contribute to the rsfMRI signal. ALFF showed the largest percentage change between measured rsfMRI metric values and residuals (>5% and <−5%) of all metrics, followed by KCC and Cohe-ReHo. fALFF, HE, and EC were all relatively unaffected by the model, with lower percentage changes. All metrics, except for EC, showed a positive percentage change in the anterior medial temporal component of the limbic network. ALFF, HE, KCC, and Cohe-ReHo showed a consistent percentage change >5% in the posterior temporal component of the frontoparietal, ventral attention, and limbic networks. The anterior component of superior, middle, and inferior temporal gyri showed a change of >5% and <−5% in ALFF, >−5% in Cohe-ReHo and EC, while KCC-ReHo also demonstrated a negative change in this area. HE was the only metric with a positive percent change in this region. The posterior medial component of the default mode network also showed a positive change >5% for ALFF, KCC, and Cohe-ReHo.

10970193, 0, Downloaded from https://onlinelibrary.wiley.com/doi/10.1002/hbm.26431 by MPI 374 Human Cognitive and Brain Sciences, Wiley Online Library on [23/08/2023]. See the Terms and Conditions (https://onlinelibrary.wiley.com/terms-and-conditions) on Wiley Online Library for rules of use; OA articles are governed by the applicable Creative Commons License

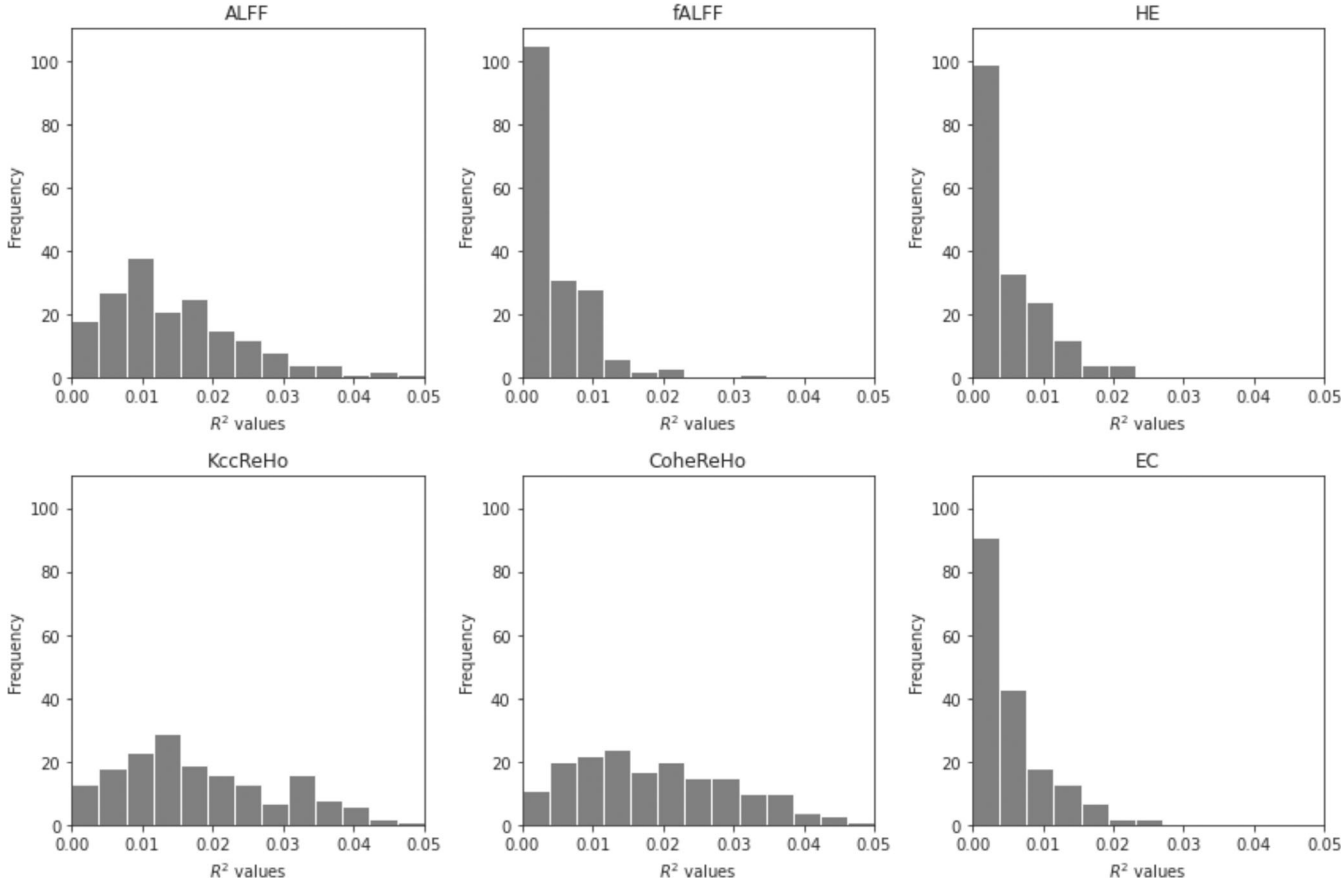

FIGURE 7 Histogram of R^2 values, which were calculated using the coefficient of determination. The R^2 values were calculated voxel-wise between measured rsfMRI values and the predicted rsfMRI metric values from the group-based model. The voxel-wise R^2 values show the fit of the model to the data and demonstrate that while some of the data is explained by the presence of veins, other aspects of physiology contribute to the rsfMRI metrics.

4 | DISCUSSION

Here we present results showing the effect of vein diameter and distance to veins on six rsfMRI metrics (ALFF, fALFF, KCC-ReHo, CoheReHo, HE, and EC) over the GM and in seven rsfMRI networks (visual, somatomotor, dorsal attention, ventral attention, limbic, frontoparietal, and default). Our findings indicate that the presence of veins introduces a systematic gradient across these common local rsfMRI metrics. The most prominent venous bias identified here was that, across most metrics and networks, values were highest near small veins, becoming lower close to large veins and decreasing further with increasing distance to larger veins. The averaged bias values were used to generate polynomial models to correct for these effects. The high R^2 values of the model on binned data indicate a good fit of the relationship between veins and metrics pooled across brain regions, days, and participants. However, on a voxel-wise level, the low R^2 values and the 2D histograms indicate that not everything can be explained by the model, and although regional vascular organization results in systematic differences, the overall patterns of the different metrics are still largely independent of venous bias. Overall, we show that network properties and connectivity can be affected by venous biases that are especially prominent near large veins and should therefore be interpreted with caution or corrected using our model. The extent of this bias is limited and dependent on the metric used, with ALFF being the most affected (average percentage change across the cortex: 0.73%) and fALFF, and HE the least affected (average percentage change across the cortex: 0.03%, −0.19%, respectively). Overall, our data, therefore, supports the presence of a bias from venous proximity and larger venous sizes, though our results are consistent with rsfMRI being predominantly a reflection of other physiological properties relevant to connectivity and metabolism.

4.1 | Vein properties

The propagated diameter map (Figure 4) shows that most voxels are located closest to veins of small diameters (<0.48 mm). This is expected as most veins in the brain are small and there are fewer larger veins (Duvernoy et al., 1981). This finding is also partially the result of the diameter distribution of the segmented veins. The mean and standard deviation of the diameter of segmented veins of all participants and days is 1.05 ± 0.61 (standard deviation of the mean

10970193, 0, Downloaded from https://onlinelibrary.wiley.com/doi/10.1002/hbm.26431 by MPI 374 Human Cognitive and Brain Sciences, Wiley Online Library on [23/08/2023]. See the Terms and Conditions (https://onlinelibrary.wiley.com/terms-and-conditions) on Wiley Online Library for rules of use; OA articles are governed by the applicable Creative Commons License

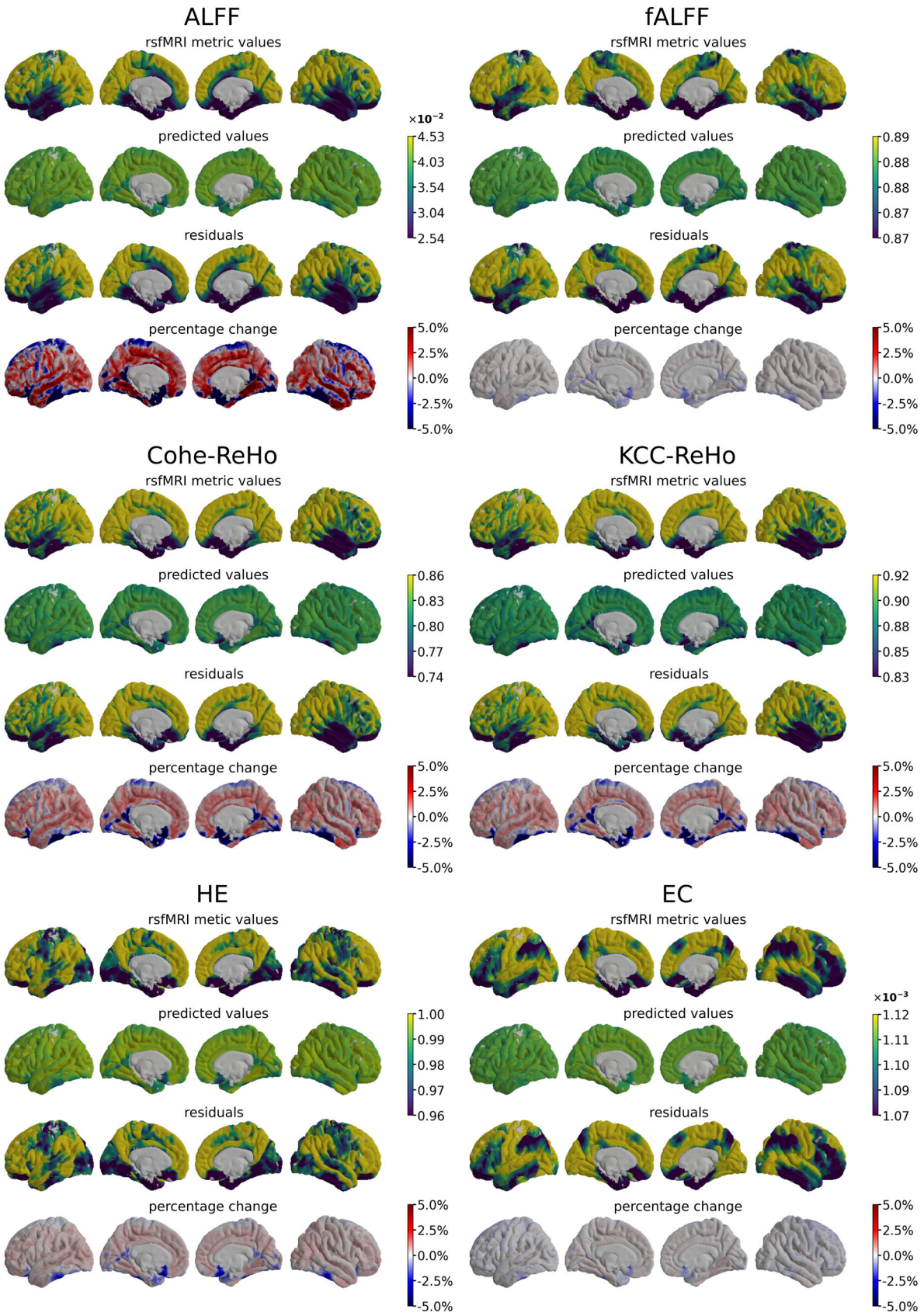

FIGURE 8 Voxel-wise rsfMRI metric values (first row), predicted (second row), residuals (third row), and percentage change between the original rsfMRI metric values and the predicted values (fourth row) for ALFF, fALFF, HE, KCC-ReHo, Cohe-ReHo, and EC. Mean GM value was added back to the residuals for visualization only, to bring all quantities on the same scale. The percentage change shows the bias caused by the veins on the different rsfMRI metrics. Veins cause the largest bias on ALFF and the lowest bias on HE and EC.

10970193, 0, Downloaded from https://onlinelibrary.wiley.com/doi/10.1002/hbm.26431 by MPI 374 Human Cognitive and Brain Sciences, Wiley Online Library on [23/08/2023]. See the Terms and Conditions (https://onlinelibrary.wiley.com/terms-and-conditions) on Wiley Online Library for rules of use; OA articles are governed by the applicable Creative Commons License

diameter across participants: 0.03). It is important to note that while sinuses have diameters >4.8 mm (Larson et al., 2020), most of these veins are located outside the cortex and were partially cropped to avoid air-tissue artifacts in the QSM reconstruction used to detect veins (Fang et al., 2017). The seemingly uniform vein diameter distribution over most cortical voxels is likely attributable to averaging over the highly variable venous architecture (in size and location as well as connections to other veins) across individuals as indicated by inter-subject variability in Figure 2 (see also Bernier et al., 2018b; Duvernoy et al., 1981; Rhoton, 2002). Larger veins have been shown to have a more consistent location (Bernier et al., 2018a), which is reflected in our data by the presence of regions with larger average diameters across participants. For example, larger average diameters in the posterior medial component of the default mode network and visual network could be caused by their proximity to the straight sinus. Large diameter veins in the posterior temporal component of the frontoparietal, ventral attention and limbic system, the anterior ventral component of the default mode network, and the posterior occipital component of the visual network could be due to the transverse sinus.

The distance map shows that sulcal voxels are typically located closer to veins (lower values) compared to gyral voxels (higher values; Figure 4). This is consistent with post-mortem observations showing that the superficial veins we most likely detect here mainly follow fissures or sulci, though some do pass across gyri (Mancall et al., 2011). Furthermore, while Duvernoy et al. report a thin, delicate venous network covering the surface of gyri, superficial veins were removed as part of the preprocessing. The largest veins Duvernoy et al. described on gyri had diameters of 280–300 μm (Auer & Loew, 1983) but these veins would be too small to be detectable or at the detection limit with the resolution used here.

4.2 | Venous bias model

The binned data (Figure 5) show the presence of a systematic venous bias on rsfMRI metrics. This is consistent with evidence that veins lead to uncertainty in the true location of fMRI signals (Menon, 2012; R. Turner, 2002; Ugurbil, 2016). Previous research has shown that the vasculature influences rsfMRI connectivity of BOLD timeseries in several ways, including increases in spurious anti-correlations and negative BOLD signal in regions close to large veins in rest conditions (Bianciardi et al., 2011; Curtis et al., 2014; Olbrich et al., 2009). Furthermore, Kay et al. (2019) showed that BOLD measurements are systematically influenced by cortical depth and curvature, indicating an effect of vein orientation in relation to the main magnetic field (Gagnon et al., 2015; Huber et al., 2017; Markuerkiaga et al., 2016). These venous influences may affect the computations of any rsfMRI metric, though the amplitude of this effect is currently unknown. While previous findings mostly focused on voxels in and directly adjacent to veins, we extend those findings to show a gradient effect of the vasculature up to 6.7 mm away from the vein. Hence, our data provide evidence for a more extensive venous influence on rsfMRI metrics from surrounding veins, which may affect all GM regions.

The underlying mechanism driving this gradient venous bias effect is likely related to blood volume and deoxyhemoglobin concentration effects in large veins, with the strongest effects occurring in voxels with high proportions of venous blood (Bianciardi et al., 2011). These effects are expected to be exacerbated in voxels containing larger draining veins, because these reflect oxygen accumulation from further away rather than a BOLD response from surrounding neural tissue (R. Turner, 2002). Here all metrics were found to be higher in and close to smaller veins, as compared to larger ones (Figure 5). Using the formula ($y = 35d_{\upsilon}^{1.5}$ with y = distance, d_v = diameter of veins) from R. Turner (2002), veins with a diameter between 0.3 and 2.5 mm drain tissue from a distance up to 5.75–138.35 mm, respectively. Therefore, the signal measured from larger veins arises from a larger area, while the signal for smaller veins is more local. For larger veins, averaging contributions from several local areas could result in a dampening effect on local fluctuations, leading to a lowering of the amplitude of most metrics. Further, some of the larger veins detected here are located in regions prone to signal loss, additionally contributing to reduced rsfMRI-derived values.

At larger distances, similarly, higher values were detected away from small veins, but lower values for larger veins. This phenomenon may partly be because we cannot detect the numerous veins that are smaller than 0.3 mm (Bollmann et al., 2022). Since the vascular tree is composed of progressively smaller veins at each branching point, a large number of voxels are likely located closer to a vein smaller than 0.3 mm. However, since we cannot detect these veins, these voxels will be classified as being closest to one of the smaller veins detected by our technique (0.3–0.5 mm) because these veins are more ubiquitous in our maps. Therefore, the distance measure for the smaller veins detected here may in part reflect an integration of the contribution of a large number of smaller undetected veins within an area of 5.75 mm (R. Turner, 2002). This could mask distance effects similar to those of larger veins, since the distance detected may not accurately reflect the actual distance to a vein in instances where a smaller vein is close-by but not detected. This effect is likely to be less present for the larger vein sizes detected here since our ability to accurately detect nearby smaller branching veins means that voxels are therefore more likely to be classified as being closer to those smaller branching veins. This hypothesis is consistent with the fact that fewer voxels are detected further from veins with larger diameters. In addition to these effects, we found that KCC-ReHo and Cohe-ReHo also have low values close to larger veins. ReHo is based on regional homogeneity, and since larger veins contain more dHb with a larger susceptibility shift (He & Yablonskiy, 2007), larger veins could therefore have a stronger effect on these metrics (Kay et al., 2019).

To evaluate if the systematic biases described above can be predicted by a simple model, the binned rsfMRI metric data were used to generate higher-order polynomial models. This model can be used in the future to correct for the systematic bias caused by veins on ALFF, fALFF, HE, KCC-ReHo, Cohe-ReHo, and EC, if venous maps are available. An alternative could be to use venous atlases (Bernier et al., 2018b; Huck et al., 2019; Ward et al., 2018) to identify the local venous properties to be entered into the model.

10970193, 0, Downloaded from https://onlinelibrary.wiley.com/doi/10.1002/hbm.26431 by MPI 374 Human Cognitive and Brain Sciences, Wiley Online Library on [23/08/2023]. See the Terms and Conditions (https://onlinelibrary.wiley.com/terms-and-conditions) on Wiley Online Library for rules of use; OA articles are governed by the applicable Creative Commons License

4.3 | Voxel-wise venous bias

To evaluate the model and to estimate the venous bias locally, the model was applied voxel-wise. Figure 6 depicts the 2D histogram showing the relationship between the voxel-wise measure rsfMRI and predicted values. As the model only captures the average influence of veins and does not capture other aspects of the BOLD signal, the range of predicted variations is narrower than measured values. This is an indication that the data is only partly biased by the presence of veins and still predominantly reflects the relevant physiological sources the rsfMRI is used to measure, such as neuronal activity fluctuations. To understand the spatial pattern of these relationships we plotted the voxel-wise averaged rsfMRI metrics, predicted values from the model, and residual values on the brain surface in Figure 8. Unlike the binned predicted values, which looked similar to the binned measure rsfMRI values, the voxel-wise averaged predicted values show a more uniform distribution with little spatial variability. This is likely related to the diameter distributions of the veins (Figure 4). Because the average venous diameter detected in most voxels is small and fairly uniform across the brain, the predicted values are mainly computed from these small veins, and therefore, the residuals show the same pattern as the original rsfMRI metrics values. This indicates that while the model captures a systematic venous bias, much of the spatial variability in rsfMRI remains intact. Therefore, the overall spatial patterns of the metrics cannot be explained by the venous bias identified here, but are related to other physiological components captured by the rsfMRI metrics, such as regional differences in neuronal activity fluctuations, validating the use of rsfMRI despite the presence of this venous bias.

The percentage change between the residuals (which have been corrected for venous effects) and the measure rsfMRI metric values was calculated and mapped onto the brain to quantify the influence of veins on the different rsfMRI metrics and show its spatial pattern. The metrics with the highest percentage change are ALFF, KCC-ReHo, and Cohe-ReHo with changes exceeding ±5%. These metrics show higher percentage changes in the regions where veins with diameters above 0.5 mm were detected. Figure 8 shows that the larger venous-related changes are located in the vicinity of the larger veins such as the great cerebral vein (vein of Galen), the sagittal sinus, and the transverse sinus. This is consistent with the fact that these larger veins collect blood from large areas, so while their BOLD dynamic range is larger, the data presented here suggest that the effect of large veins on these metrics may be predominantly related to a dampening effect from the influence of several regions with potentially different patterns of fluctuations. While KCC-ReHo and Cohe-ReHo show smaller percentage changes than ALFF, the areas with the highest changes are located in similar regions, indicating that the two ReHo methods are similarly affected by the venous bias identified here.

EC and HE show lower percentage changes than both ReHo metrics and ALFF throughout the brain, with most changes below |5|%. However, one area of the right temporal lobe shows percentage changes above 5% (EC and HE) and below −5% (EC). Although high percentage changes were also observed in the temporal lobe with ALFF and ReHo, the laterality of the effect was not as prominent. These temporal lobe effects may be because we acquired our data on a head-only 7 T MRI machine, which are known to suffer more from field inhomogeneities and signal loss than lower field magnets (Abduljalil & Robitaille, 1999; Yang et al., 2006), especially at the edge of the magnetic field. Since this was a head-only system, the edge of the uniform field was therefore close to the lower temporal lobe. To alleviate these effects, piezoelectric pads were used at the base of the head (O'Reilly et al., 2016), but the placement of these pads may not have been optimal for all participants or not enough to reliably improve field homogeneity around the temporal lobe.

Since the percentage change in fALFF was lower than the percentage change in HE, fALFF may be one of the metrics least biased by the presence of veins. Interestingly, ALFF shows the highest percentage change, the large difference between the two related metrics is likely because fALFF is a ratio measure, and the venous bias may be similar across all or multiple frequencies. Taking the ratio of the power spectrum of low-frequency (0.01–0.1 Hz) to that of the entire frequency range will lessen the metric's dependence on the amplitude of the BOLD signal, and therefore reduce the venous bias. This is consistent with previous findings, showing that fALFF effectively suppresses nonspecific signal components and provides an improved sensitivity and specificity in the detection of spontaneous regional brain activation (Zou et al., 2008). Consistent with this, HE shows a similarly low venous bias since it is based on self-similarity across different scales, and is therefore also less dependent on the amplitude of the signal per se. The other metrics examined here are more directly dependent on the amplitude of the signal.

In summary, while the model demonstrates a high fit on binned data, indicating the presence of a systematic bias that can be captured by a fairly simple polynomial model, a large proportion of the variability in rsfMRI metrics at the voxel-wise level remains intact, indicating that this bias is modest at the voxel-wise level and therefore not the dominant source of contrast for these metrics. While some metrics (ALFF, Cohe-ReHo, and KCC-ReHo) have a stronger venous bias than others (fALFF, HE, and EC), the overall impact of veins on BOLD-derived rsfMRI metrics is small. In addition, the model proposed here can be used to remove this bias, either by vein segmentation or with a venous atlas, and can improve the accuracy of rsfMRI quantifications.

4.4 | Limitations

The main limitation of this work is related to resolution, both the QSM images and the rsfMRI images. While acquiring this data on an ultra-high field 7 T Magnetic Resonance Imaging (MRI) scanner allowed us to acquire the GRE sequence with a 0.6 mm isotropic resolution, it was still only possible to measure relatively large veins (>0.3 mm). These veins can drain an area up to 5.75 mm. This is problematic for the bias calculation, because a part of the bias in BOLD arises from smaller veins. The resolution of the rsfMRI data was coarser than that of the QSM, with a voxel size of 1.2 mm isotropic. A

10970193, 0, Downloaded from https://onlinelibrary.wiley.com/doi/10.1002/hbm.26431 by MPI 374 Human Cognitive and Brain Sciences, Wiley Online Library on [23/08/2023]. See the Terms and Conditions (https://onlinelibrary.wiley.com/terms-and-conditions) on Wiley Online Library for rules of use; OA articles are governed by the applicable Creative Commons License

higher resolution would alleviate some of these effects and lead to a more accurate model of the relationship between rsfMRI and venous proximity and size. However, the resolution for the GRE and BOLD sequences is limited by acquisition time and participant movement, especially for QSM data.

The quality of the model is dependent on the quality of the QSM reconstruction and in turn on our ability to detect a comprehensive vascular tree. There are many different QSM reconstruction methods available, each of which can lead to a different number of detected vessels, and with various sensitivity to detect veins at the cortical surface (Berg et al., 2021; Biondetti et al., 2020). Here we used TGV-QSM (Langkammer et al., 2015) because it was found to yield the largest number of veins, but at this resolution and data quality, the vascular tree remains incomplete with disconnected vessel segments. Because QSM is an ill-posed problem, some veins are not fully detectable depending on their orientation to the main magnetic field (Fan et al., 2014). This means that even though the distance maps and the propagated diameter maps were used, the closest identified vein may not in fact be the closest vein if venous segments were not detected in our QSM. Future studies could seek to use multiple head orientations for their QSM to alleviate some of these issues, though the use of multiple orientations significantly increases the length and difficulty of the acquisition.

Here, the venous bias affecting six different rsfMRI metrics were calculated. Other rsfMRI metrics exist and could be investigated in this manner, to create correction models for the effects of venous proximity and size. While the list used here is not complete, it includes a variety of local metrics, which cover short-, mid-, and long-range connectivity and cover different functional connectivity analyses, like voxel-wise (ALFF, fALFF, KCC-ReHo, and Cohe-ReHo), graph-based (EC), and temporal dynamics-based (HE). Therefore, it makes a representative subset of analyses commonly used in the field, and this manuscript can be used as a blueprint for investigating the effects on other metrics.

Finally, the data used in this study was acquired on a 7 T MRI scanner. While 7 T scanners provide better signal, they are also known to have greater field inhomogeneities, especially in the temporal lobe and orbitofrontal regions. Furthermore, the models presented here may be field dependent since the effect of intravascular hemoglobin on tissue BOLD signal has been shown to be field-strength dependent (Barth & Poser, 2011; Gati et al., 1997; Triantafyllou et al., 2011). Future studies could extend our findings to 3 T to investigate potentially different effects in the temporal lobe and to create field-specific models.

ACKNOWLEDGMENTS

The authors thank Domenica Wilfling and Elisabeth Wladimirov for helping with recruitment, logistics, and data acquisition of the multimodal plasticity initiative (MMPI) dataset. This work was supported by the Max Planck Society, the Canadian Natural Sciences and Engineering Research Council (RGPIN-2015-04665, to Claudine J. Gauthier; RGPIN-2020-06812, DGECR-2020-00146, to Christopher J. Steele), the Heart and Stroke Foundation of Canada (N.I.A., to Claudine J. Gauthier; HNC 170723), the Canadian Institutes of Health Research Accelerator (N.I.A., Christopher J. Steele), the National Institute of Health (R00NS102884, to Audrey P. Fan), the Michal and Renata Hornstein Chair in Cardiovascular Imaging (to Claudine J. Gauthier), the Quebec Bio-Imaging Network (QBIN; to Julia Huck), and FRQNT (to Julia Huck, Christopher J. Steele).

CONFLICT OF INTEREST STATEMENT

The authors declare no conflicts of interest.

DATA AVAILABILITY STATEMENT

The ethics for this project does not allow for data sharing with external researchers.

ORCID

Julia Huck https://orcid.org/0000-0002-5701-8506
Anna-Thekla Jäger https://orcid.org/0000-0002-3381-8453
Christine Tardif https://orcid.org/0000-0001-8356-6808
Arno Villringer https://orcid.org/0000-0003-2604-2404

REFERENCES

Abdelkarim, D., Zhao, Y., Turner, M. P., Sivakolundu, D. K., Lu, H., & Rypma, B. (2019). A neural-vascular complex of age-related changes in the human brain: Anatomy, physiology, and implications for neurocognitive aging. *Neuroscience & Biobehavioral Reviews*, *107*, 927–944. https://doi.org/10.1016/j.neubiorev.2019.09.005

Abduljalil, A. M., & Robitaille, P.-M. L. (1999). Macroscopic susceptibility in ultra high field MRI. *Journal of Computer Assisted Tomography*, *23*(6), 832–841. https://doi.org/10.1097/00004728-199911000-00004

Abraham, A., Pedregosa, F., Eickenberg, M., Gervais, P., Mueller, A., Kossaifi, J., Gramfort, A., Thirion, B., & Varoquaux, G. (2014). Machine learning for neuroimaging with scikit-learn. *Frontiers in Neuroinformatics*, *8*(FEB), 14. https://doi.org/10.3389/fninf.2014.00014

Auer, L. M., & Loew, F. (1983). The cerebral veins: An experimental and clinical update. https://search.ebscohost.com/login.aspx?direct=true&scope=site&db=nlebk&db=nlabk&AN=2861412

Avants, B. B., Tustison, N., & Song, G. (2009). Advanced normalization tools (ANTS). *Insight Journal*, *2*, 1–35. http://hdl.handle.net/10380/3113

Barth, M., & Poser, B. A. (2011). Advances in high-field BOLD fMRI. *Materials*, *4*(11), 1941–1955. https://doi.org/10.3390/ma4111941

Bazin, P.-L., Plessis, V., Fan, A. P., Villringer, A., & Gauthier, C. J. (2016). Vessel segmentation from quantitative susceptibility maps for local oxygenation venography. In *Proceedings of the 2016 IEEE 13th International Symposium on Biomedical Imaging* (*ISBI*), pp. 1135–1138. https://doi.org/10.1109/ISBI.2016.7493466

Behzadi, Y., Restom, K., Liau, J., & Liu, T. T. (2007). A component based noise correction method (CompCor) for BOLD and perfusion based fMRI. *NeuroImage*, *37*(1), 90–101. https://doi.org/10.1016/j.neuroimage.2007.04.042

Berg, R. C., Preibisch, C., Thomas, D. L., Shmueli, K., & Biondetti, E. (2021). Investigating the effect of flow compensation and quantitative susceptibility mapping method on the accuracy of venous susceptibility measurement. *NeuroImage*, *240*, 118399. https://doi.org/10.1016/j.neuroimage.2021.118399

Bernier, M., Cunnane, S. C., & Whittingstall, K. (2018a). The spatial distribution of arterial and venous vessels in the human brain. *Proceedings of the International Society for Magnetic Resonance in Medicine*, *1015*, 5–7.

Bernier, M., Cunnane, S. C., & Whittingstall, K. (2018b). The morphology of the human cerebrovascular system. *Human Brain Mapping*, *39*(12), 4962–4975. https://doi.org/10.1002/hbm.24337

10970193, 0, Downloaded from https://onlinelibrary.wiley.com/doi/10.1002/hbm.26431 by MPI 374 Human Cognitive and Brain Sciences, Wiley Online Library on [23/08/2023]. See the Terms and Conditions (https://onlinelibrary.wiley.com/terms-and-conditions) on Wiley Online Library for rules of use; OA articles are governed by the applicable Creative Commons License

Bianciardi, M., Fukunaga, M., Gelderen, P. V., Zwart, J. A. D., & Duyn, J. H. (2011). Negative BOLD-fMRI signals in large cerebral veins. *Journal of Cerebral Blood Flow and Metabolism*, *31*(2), 401–412. https://doi.org/10.1038/jcbfm.2010.164

Biondetti, E., Karsa, A., Thomas, D. L., & Shmueli, K. (2020). Investigating the accuracy and precision of TE-dependent versus multi-echo QSM using Laplacian-based methods at 3 T. *Magnetic Resonance in Medicine*, *84*(6), 3040–3053. https://doi.org/10.1002/mrm.28331

Biswal, B., Zerrin Yetkin, F., Haughton, V. M., & Hyde, J. S. (1995). Functional connectivity in the motor cortex of resting human brain using echo-planar MRI. *Magnetic Resonance in Medicine*, *34*(4), 537–541. https://doi.org/10.1002/mrm.1910340409

Bollmann, S., Mattern, H., Bernier, M., Robinson, S. D., Park, D., Speck, O., & Polimeni, J. R. (2022). Imaging of the pial arterial vasculature of the human brain in vivo using high-resolution 7T time-of-flight angiography. *eLife*, *11*, e71186. https://doi.org/10.7554/eLife.71186

Cetin, S., Bilgic, B., Fan, A., Holdsworth, S., & Unal, G. (2016). Vessel orientation constrained quantitative susceptibility mapping (QSM) reconstruction. In S. Ourselin, L. Joskowicz, M. R. Sabuncu, G. Unal, & W. Wells (Eds.), *Medical image computing and computer-assisted intervention—MICCAI 2016* (Vol. 9902, pp. 467–474). Springer International Publishing. https://doi.org/10.1007/978-3-319-46726-9_54

Chen, Z., Caprihan, A., & Calhoun, V. (2010). Effect of surrounding vasculature on intravoxel BOLD signal. *Medical Physics*, *37*(4), 1778–1787. https://doi.org/10.1118/1.3366251

Curtis, A. T., Hutchison, R. M., & Menon, R. S. (2014). Phase based venous suppression in resting-state BOLD GE-fMRI. *NeuroImage*, *100*, 51–59. https://doi.org/10.1016/j.neuroimage.2014.05.079

Dai, D.-F., Chen, T., Johnson, S. C., Szeto, H., & Rabinovitch, P. S. (2012). Cardiac aging: From molecular mechanisms to significance in human health and disease. *Antioxidants & Redox Signaling*, *16*(12), 1492–1526. https://doi.org/10.1089/ars.2011.4179

Deistung, A., Schäfer, A., Schweser, F., Biedermann, U., Turner, R., & Reichenbach, J. R. (2013). Toward in vivo histology: A comparison of quantitative susceptibility mapping (QSM) with magnitude-, phase-, and R_2^*-imaging at ultra-high magnetic field strength. *NeuroImage*, *65*, 299–314. https://doi.org/10.1016/j.neuroimage.2012.09.055

Drew, P. J. (2019). Vascular and neural basis of the BOLD signal. *Current Opinion in Neurobiology*, *58*, 61–69. https://doi.org/10.1016/j.conb.2019.06.004

Duvernoy, H. M., Delon, S., & Vannson, J. L. (1981). Cortical blood vessels of the human brain. *Brain Research Bulletin*, *7*(5), 519–579. https://doi.org/10.1016/0361-9230(81)90007-1

Fan, A. P., Bilgic, B., Gagnon, L., Witzel, T., Bhat, H., Rosen, B. R., & Adalsteinsson, E. (2014). Quantitative oxygenation venography from MRI phase. *Magnetic Resonance in Medicine*, *72*(1), 149–159. https://doi.org/10.1002/mrm.24918

Fan, A. P., Govindarajan, S. T., Kinkel, R. P., Madigan, N. K., Nielsen, A. S., Benner, T., Tinelli, E., Rosen, B. R., Adalsteinsson, E., & Mainero, C. (2015). Quantitative oxygen extraction fraction from 7-tesla MRI phase: Reproducibility and application in multiple sclerosis. *Journal of Cerebral Blood Flow & Metabolism*, *35*(1), 131–139. https://doi.org/10.1038/jcbfm.2014.187

Fang, J., Bao, L., Li, X., van Zijl, P. C. M., & Chen, Z. (2017). Background field removal using a region adaptive kernel for quantitative susceptibility mapping of human brain. *Journal of Magnetic Resonance*, *281*, 130–140. https://doi.org/10.1016/j.jmr.2017.05.004

Fulop, G. A., Tarantini, S., Yabluchanskiy, A., Molnar, A., Prodan, C. I., Kiss, T., Csipo, T., Lipecz, A., Balasubramanian, P., Farkas, E., Toth, P., Sorond, F., Csiszar, A., & Ungvari, Z. (2019). Role of age-related alterations of the cerebral venous circulation in the pathogenesis of vascular cognitive impairment. *American Journal of Physiology-Heart and Circulatory Physiology*, *316*(5), H1124–H1140. https://doi.org/10.1152/ajpheart.00776.2018

Gagnon, L., Sakadžić, S., Lesage, F., Musacchia, J. J., Lefebvre, J., Fang, Q., Yücel, M. A., Evans, K. C., Mandeville, E. T., Cohen-Adad, J., Polimeni, J. R., Yaseen, M. A., Lo, E. H., Greve, D. N., Buxton, R. B., Dale, A. M., Devor, A., & Boas, D. A. (2015). Quantifying the microvascular origin of BOLD-fMRI from first principles with two-photon microscopy and an oxygen-sensitive Nanoprobe. *The Journal of Neuroscience*, *35*(8), 3663–3675. https://doi.org/10.1523/JNEUROSCI.3555-14.2015

Garrett, D. D., Lindenberger, U., Hoge, R. D., & Gauthier, C. J. (2017). Age differences in brain signal variability are robust to multiple vascular controls. *Scientific Reports*, *7*(1), 10149. https://doi.org/10.1038/s41598-017-09752-7

Gati, J. S., Menon, R. S., Ugurbil, K., & Rutt, B. K. (1997). Experimental determination of the BOLD field strength dependence in vessels and tissue. *Magnetic Resonance in Medicine*, *38*(2), 296–302. https://doi.org/10.1002/mrm.1910380220

Gauthier, C. J., Madjar, C., Desjardins-Crépeau, L., Bellec, P., Bherer, L., & Hoge, R. D. (2013). Age dependence of hemodynamic response characteristics in human functional magnetic resonance imaging. *Neurobiology of Aging*, *34*(5), 1469–1485. https://doi.org/10.1016/j.neurobiolaging.2012.11.002

Gorgolewski, K., Burns, C. D., Madison, C., Clark, D., Halchenko, Y. O., Waskom, M. L., & Ghosh, S. S. (2011). Nipype: A flexible, lightweight and extensible neuroimaging data processing framework in python. *Frontiers in Neuroinformatics*, *5*, 13. https://doi.org/10.3389/fninf.2011.00013

Haase, A., Frahm, J., Matthaei, D., Hanicke, W., & Merboldt, K.-D. (1986). FLASH imaging. Rapid NMR imaging using low flip-angle pulses. *Journal of Magnetic Resonance (1969)*, *67*(2), 258–266. https://doi.org/10.1016/0022-2364(86)90433-6

Hammond, K. E., Lupo, J. M., Xu, D., Metcalf, M., Kelley, D. A. C., Pelletier, D., Chang, S. M., Mukherjee, P., Vigneron, D. B., & Nelson, S. J. (2008). Development of a robust method for generating 7.0 T multichannel phase images of the brain with application to normal volunteers and patients with neurological diseases. *NeuroImage*, *39*(4), 1682–1692. https://doi.org/10.1016/j.neuroimage.2007.10.037

Hardstone, R., Poil, S. S., Schiavone, G., Jansen, R., Nikulin, V. V., Mansvelder, H. D., & Linkenkaer-Hansen, K. (2012). Detrended fluctuation analysis: A scale-free view on neuronal oscillations. *Frontiers in Physiology*, *3*, 450. https://doi.org/10.3389/fphys.2012.00450

He, X., & Yablonskiy, D. A. (2007). Quantitative BOLD: Mapping of human cerebral deoxygenated blood volume and oxygen extraction fraction: Default state. *Magnetic Resonance in Medicine*, *57*(1), 115–126. https://doi.org/10.1002/mrm.21108

Hsieh, M.-C., Tsai, C.-Y., Liao, M.-C., Yang, J.-L., Su, C.-H., & Chen, J.-H. (2016). Quantitative susceptibility mapping-based microscopy of magnetic resonance venography (QSM-mMRV) for In vivo morphologically and functionally assessing Cerebromicrovasculature in rat stroke model. *PLOS One*, *11*(3), e0149602. https://doi.org/10.1371/journal.pone.0149602

Huber, L., Handwerker, D. A., Jangraw, D. C., Chen, G., Hall, A., Stüber, C., Gonzalez-Castillo, J., Ivanov, D., Marrett, S., Guidi, M., Goense, J., Poser, B. A., & Bandettini, P. A. (2017). High-resolution CBV-fMRI allows mapping of laminar activity and connectivity of cortical input and output in human M1. *Neuron*, *96*(6), 1253–1263.e7. https://doi.org/10.1016/j.neuron.2017.11.005

Huck, J., Wanner, Y., Fan, A. P., Jäger, A. T., Grahl, S., Schneider, U., Villringer, A., Steele, C. J., Tardif, C. L., Bazin, P. L., & Gauthier, C. J. (2019). High resolution atlas of the venous brain vasculature from 7 T quantitative susceptibility maps. *Brain Structure and Function*, *224*(7), 2467–2485. https://doi.org/10.1007/s00429-019-01919-4

Huntenburg, J. M., Steele, C. J., & Bazin, P.-L. (2018). Nighres: Processing tools for high-resolution neuroimaging. *GigaScience*, *7*(7), giy082. https://doi.org/10.1093/gigascience/giy082

10970193, 0, Downloaded from https://onlinelibrary.wiley.com/doi/10.1002/hbm.26431 by MPI 374 Human Cognitive and Brain Sciences, Wiley Online Library on [23/08/2023]. See the Terms and Conditions (https://onlinelibrary.wiley.com/terms-and-conditions) on Wiley Online Library for rules of use; OA articles are governed by the applicable Creative Commons License

Hurst, H. E. (1951). Long-term storage capacity of reservoirs. *Transactions of the American Society of Civil Engineers*, *116*(1), 770–799. https://doi.org/10.1061/TACEAT.0006518

Jäger, A.-T. P., Huntenburg, J. M., Tremblay, S. A., Schneider, U., Grahl, S., Huck, J., Tardif, C. L., Villringer, A., Gauthier, C. J., Bazin, P.-L., & Steele, C. J. (2021). Motor sequences; separating the sequence from the motor. A longitudinal rsfMRI study. *Brain Structure and Function*, *227*, 793–807. https://doi.org/10.1007/s00429-021-02412-7

Jenkinson, M., Bannister, P., Brady, M., & Smith, S. (2002). Improved optimization for the robust and accurate linear registration and motion correction of brain images. *NeuroImage*, *17*(2), 825–841. https://doi.org/10.1006/nimg.2002.1132

Jiao, F., Gao, Z., Shi, K., Jia, X., Wu, P., Jiang, C., Ge, J., Su, H., Guan, Y., Shi, S., Zang, Y.-F., & Zuo, C. (2019). Frequency-dependent relationship between resting-state fMRI and glucose metabolism in the elderly. *Frontiers in Neurology*, *10*, 566. https://doi.org/10.3389/fneur.2019.00566

Kalcher, K., Boubela, R. N., Huf, W., Našel, C., & Moser, E. (2015). Identification of voxels confounded by venous signals using resting-state fMRI functional connectivity graph community identification. *Frontiers in Neuroscience*, *9*, 472. https://doi.org/10.3389/fnins.2015.00472

Kannurpatti, S. S., Motes, M. A., Rypma, B., & Biswal, B. B. (2010). Neural and vascular variability and the fMRI-BOLD response in normal aging. *Magnetic Resonance Imaging*, *28*(4), 466–476. https://doi.org/10.1016/j.mri.2009.12.007

Kay, K., Jamison, K. W., Vizioli, L., Zhang, R., Margalit, E., & Ugurbil, K. (2019). A critical assessment of data quality and venous effects in sub-millimeter fMRI. *NeuroImage*, *189*, 847–869. https://doi.org/10.1016/j.neuroimage.2019.02.006

Keuken, M. C., Bazin, P.-L., Crown, L., Hootsmans, J., Laufer, A., Müller-Axt, C., Sier, R., van der Putten, E. J., Schäfer, A., Turner, R., & Forstmann, B. U. (2014). Quantifying inter-individual anatomical variability in the subcortex using 7 T structural MRI. *NeuroImage*, *94*, 40–46. https://doi.org/10.1016/j.neuroimage.2014.03.032

Langkammer, C., Bredies, K., Poser, B. A., Barth, M., Reishofer, G., Fan, A. P., Bilgic, B., Fazekas, F., Mainero, C., & Ropele, S. (2015). Fast quantitative susceptibility mapping using 3D EPI and total generalized variation. *NeuroImage*, *111*, 622–630. https://doi.org/10.1016/j.neuroimage.2015.02.041

Larson, A. S., Lanzino, G., & Brinjikji, W. (2020). Variations of intracranial dural venous sinus diameters from birth to 20 years of age: An MRV-based study. *American Journal of Neuroradiology*, *41*(12), 2351–2357. https://doi.org/10.3174/ajnr.A6816

Lee, M. H., Smyser, C. D., & Shimony, J. S. (2013). Resting-state fMRI: A review of methods and clinical applications. *American Journal of Neuroradiology*, *34*(10), 1866–1872. https://doi.org/10.3174/ajnr.A3263

Liu, Z., & Li, Y. (2016). Cortical cerebral blood flow, oxygen extraction fraction, and metabolic rate in patients with middle cerebral artery stenosis or acute stroke. *American Journal of Neuroradiology*, *37*(4), 607–614. https://doi.org/10.3174/ajnr.A4624

Logothetis, N. K., & Wandell, B. A. (2004). Interpreting the BOLD signal. *Annual Review of Physiology*, *66*(1), 735–769. https://doi.org/10.1146/annurev.physiol.66.082602.092845

Lohmann, G., Margulies, D. S., Horstmann, A., Pleger, B., Lepsien, J., Goldhahn, D., Schloegl, H., Stumvoll, M., Villringer, A., & Turner, R. (2010). Eigenvector centrality mapping for analyzing connectivity patterns in fMRI data of the human brain. *PLoS One*, *5*(4), e10232. https://doi.org/10.1371/journal.pone.0010232

Mancall, E. L., Brock, D. G., & Gray, H. (2011). *Gray's clinical neuroanatomy the anatomic basis for clinical neuroscience*. Elsevier/Saunders http://www.clinicalkey.com/dura/browse/bookChapter/3-s2.0-C20090373134.

Manera, A. L., Dadar, M., Collins, D. L., & Ducharme, S. (2019). Deformation based morphometry study of longitudinal MRI changes in behavioral variant frontotemporal dementia. *NeuroImage: Clinical*, *24*, 102079. https://doi.org/10.1016/j.nicl.2019.102079

Markuerkiaga, I., Barth, M., & Norris, D. G. (2016). A cortical vascular model for examining the specificity of the laminar BOLD signal. *NeuroImage*, *132*, 491–498. https://doi.org/10.1016/j.neuroimage.2016.02.073

Marques, J. P., Kober, T., Krueger, G., van der Zwaag, W., Van de Moortele, P.-F., & Gruetter, R. (2010). MP2RAGE, a self bias-field corrected sequence for improved segmentation and T1-mapping at high field. *NeuroImage*, *49*(2), 1271–1281. https://doi.org/10.1016/j.neuroimage.2009.10.002

Menon, R. S. (2012). The great brain versus vein debate. *NeuroImage*, *62*(2), 970–974. https://doi.org/10.1016/j.neuroimage.2011.09.005

Millman, K. J., & Brett, M. (2007). Analysis of functional magnetic resonance imaging in python. *Computing in Science and Engineering*, *9*(3), 52–55. https://doi.org/10.1109/MCSE.2007.46

Olbrich, S., Mulert, C., Karch, S., Trenner, M., Leicht, G., Pogarell, O., & Hegerl, U. (2009). EEG-vigilance and BOLD effect during simultaneous EEG/fMRI measurement. *NeuroImage*, *45*(2), 319–332. https://doi.org/10.1016/j.neuroimage.2008.11.014

O'Reilly, T. P. A., Webb, A. G., & Brink, W. M. (2016). Practical improvements in the design of high permittivity pads for dielectric shimming in neuroimaging at 7 T. *Journal of Magnetic Resonance*, *270*, 108–114. https://doi.org/10.1016/j.jmr.2016.07.003

Paneni, F., Diaz Cañestro, C., Libby, P., Lüscher, T. F., & Camici, G. G. (2017). The aging cardiovascular system. *Journal of the American College of Cardiology*, *69*(15), 1952–1967. https://doi.org/10.1016/j.jacc.2017.01.064

Peng, C.-K., Buldyrev, S. V., Havlin, S., Simons, M., Stanley, H. E., & Goldberger, A. L. (1994). Mosaic organization of DNA nucleotides. *Physical Review E*, *49*(2), 1685–1689. https://doi.org/10.1103/PhysRevE.49.1685

Plante, G. E. (2002). Vascular response to stress in health and disease. *Metabolism*, *51*(6PB), 25–30.

Poser, B. A., Koopmans, P. J., Witzel, T., Wald, L. L., & Barth, M. (2010). Three dimensional echo-planar imaging at 7 tesla. *NeuroImage*, *51*(1), 261–266. https://doi.org/10.1016/j.neuroimage.2010.01.108

Rhoton, A. L. (2002). The Supratentorial cranial space: Microsurgical anatomy and surgical approaches. *Neurosurgery*, *51*(suppl_4), S1-iii–S1-vi. https://doi.org/10.1097/00006123-200210001-00001

Roche, A. (2011). A four-dimensional registration algorithm with application to joint correction of motion and slice timing in fMRI. *IEEE Transactions on Medical Imaging*, *30*(8), 1546–1554. https://doi.org/10.1109/TMI.2011.2131152

Song, X.-W., Dong, Z.-Y., Long, X.-Y., Li, S.-F., Zuo, X.-N., Zhu, C.-Z., He, Y., Yan, C.-G., & Zang, Y.-F. (2011). REST: A toolkit for resting-state functional magnetic resonance imaging data processing. *PLoS ONE*, *6*(9), e25031. https://doi.org/10.1371/journal.pone.0025031

Sweeney, M. D., Kisler, K., Montagne, A., Toga, A. W., & Zlokovic, B. V. (2018). The role of brain vasculature in neurodegenerative disorders. *Nature Neuroscience*, *21*(10), 1318–1331. https://doi.org/10.1038/s41593-018-0234-x

Tremblay, S. A., Jäger, A.-T., Huck, J., Giacosa, C., Beram, S., Schneider, U., Grahl, S., Villringer, A., Tardif, C. L., Bazin, P.-L., Steele, C. J., & Gauthier, C. J. (2021). White matter microstructural changes in short-term learning of a continuous visuomotor sequence. *Brain Structure and Function*, *226*(6), 1677–1698. https://doi.org/10.1007/s00429-021-02267-y

Triantafyllou, C., Wald, L. L., & Hoge, R. D. (2011). Echo-time and field strength dependence of BOLD reactivity in veins and parenchyma using flow-normalized Hypercapnic manipulation. *PLoS One*, *6*(9), e24519. https://doi.org/10.1371/journal.pone.0024519

Tsvetanov, K. A., Henson, R. N. A., & Rowe, J. B. (2021). Separating vascular and neuronal effects of age on fMRI BOLD signals. *Philosophical Transactions of the Royal Society B: Biological Sciences*, *376*(1815), 20190631. https://doi.org/10.1098/rstb.2019.0631

10970193, 0, Downloaded from https://onlinelibrary.wiley.com/doi/10.1002/hbm.26431 by MPI 374 Human Cognitive and Brain Sciences, Wiley Online Library on [23/08/2023]. See the Terms and Conditions (https://onlinelibrary.wiley.com/terms-and-conditions) on Wiley Online Library for rules of use; OA articles are governed by the applicable Creative Commons License

Turner, J. A. (2013). A multi-site resting state fMRI study on the amplitude of low frequency fluctuations in schizophrenia. *Frontiers in Neuroscience*, *7*, 137. https://doi.org/10.3389/fnins.2013.00137

Turner, R. (2002). How much codex can a vein drain? Downstream dilution of activation-related cerebral blood oxygenation changes. *NeuroImage*, *16*(4), 1062–1067. https://doi.org/10.1006/nimg.2002.1082

Ugurbil, K. (2016). What is feasible with imaging human brain function and connectivity using functional magnetic resonance imaging. *Philosophical Transactions of the Royal Society B: Biological Sciences*, *371*(1705), 20150361. https://doi.org/10.1098/rstb.2015.0361

Vigneau-Roy, N., Bernier, M., Descoteaux, M., & Whittingstall, K. (2014). Regional variations in vascular density correlate with resting-state and task-evoked blood oxygen level-dependent signal amplitude: Correlation between vascular density and BOLD amplitude. *Human Brain Mapping*, *35*(5), 1906–1920. https://doi.org/10.1002/hbm.22301

Wang, Y., & Liu, T. (2015). Quantitative susceptibility mapping (QSM): Decoding MRI data for a tissue magnetic biomarker. *Magnetic Resonance in Medicine*, *73*(1), 82–101. https://doi.org/10.1002/mrm.25358

Ward, P. G. D., Ferris, N. J., Raniga, P., Dowe, D. L., Ng, A. C. L., Barnes, D. G., & Egan, G. F. (2018). Combining images and anatomical knowledge to improve automated vein segmentation in MRI. *NeuroImage*, *165*, 294–305. https://doi.org/10.1016/j.neuroimage.2017.10.049

Winder, A. T., Echagarruga, C., Zhang, Q., & Drew, P. J. (2017). Weak correlations between hemodynamic signals and ongoing neural activity during the resting state. *Nature Neuroscience*, *20*(12), 1761–1769. https://doi.org/10.1038/s41593-017-0007-y

Wink, A. M., van der Werf, Y. D., van den Heuvel, O. A., Barkhof, F., & de Munck, J. C. (2012). Fast eigenvector centrality mapping of voxel-wise connectivity in functional magnetic resonance imaging: Implementation, validation, and interpretation. *Brain Connectivity*, *2*, 265–274. https://doi.org/10.1089/brain.2012.0087

Woerz, S., & Rohr, K. (2004). A new 3D parametric intensity model for accurate segmentation and quantification of human vessels. In C. Barillot, D. R. Haynor, & P. Hellier (Eds.), *Medical image computing and computer-assisted intervention (MICCAI 2004). Lecture Notes in Computer Science* (Vol. 3216, pp. 491–499). Springer.

Xu, X., Wang, B., Ren, C., Hu, J., Greenberg, D. A., Chen, T., Xie, L., & Jin, K. (2017). Age-related impairment of vascular structure and functions. *Aging and Disease*, *8*(5), 590–610. https://doi.org/10.14336/AD.2017.0430

Yang, Q. X., Smith, M. B., & Wang, J. (2006). Magnetic susceptibility effects in high field MRI. In *Ultra high field magnetic resonance imaging* (Vol. 26, pp. 249–284). Springer US. https://doi.org/10.1007/978-0-387-49648-1_9

Yeo, T. B. T., Krienen, F. M., Sepulcre, J., Sabuncu, M. R., Lashkari, D., Hollinshead, M., Roffman, J. L., Smoller, J. W., Zöllei, L., Polimeni, J. R., Fischl, B., Liu, H., & Buckner, R. L. (2011). The organization of the human cerebral cortex estimated by intrinsic functional connectivity. *Journal of Neurophysiology*, *106*(3), 1125–1165. https://doi.org/10.1152/jn.00338.2011

Zang, Y., Jiang, T., Lu, Y., He, Y., & Tian, L. (2004). Regional homogeneity approach to fMRI data analysis. *NeuroImage*, *22*(1), 394–400. https://doi.org/10.1016/j.neuroimage.2003.12.030

Zang, Y.-F., He, Y., Zhu, C.-Z., Cao, Q.-J., Sui, M.-Q., Liang, M., Tian, L.-X., Jiang, T.-Z., & Wang, Y.-F. (2007). Altered baseline brain activity in children with ADHD revealed by resting-state functional MRI. *Brain & Development*, *29*(2), 83–91. https://doi.org/10.1016/j.braindev.2006.07.002

Zou, Q.-H., Zhu, C.-Z., Yang, Y., Zuo, X.-N., Long, X.-Y., Cao, Q.-J., Wang, Y.-F., & Zang, Y.-F. (2008). An improved approach to detection of amplitude of low-frequency fluctuation (ALFF) for resting-state fMRI: Fractional ALFF. *Journal of Neuroscience Methods*, *172*(1), 137–141. https://doi.org/10.1016/j.jneumeth.2008.04.012

SUPPORTING INFORMATION

Additional supporting information can be found online in the Supporting Information section at the end of this article.

How to cite this article: Huck, J., Jäger, A.-T., Schneider, U., Grahl, S., Fan, A. P., Tardif, C., Villringer, A., Bazin, P.-L., Steele, C. J., & Gauthier, C. J. (2023). Modeling venous bias in resting state functional MRI metrics. *Human Brain Mapping*, 1–18. https://doi.org/10.1002/hbm.26431

10970193, 0, Downloaded from https://onlinelibrary.wiley.com/doi/10.1002/hbm.26431 by MPI 374 Human Cognitive and Brain Sciences, Wiley Online Library on [23/08/2023]. See the Terms and Conditions (https://onlinelibrary.wiley.com/terms-and-conditions) on Wiley Online Library for rules of use; OA articles are governed by the applicable Creative Commons License